Near-real-time global biomass burning emissions product from geostationary satellite constellation

Xiaoyang Zhang,[1,2] Shobha Kondragunta,[2] Jessica Ram,[3] Christopher Schmidt,[4] and Ho-Chun Huang[5]

Received 9 January 2012; revised 29 May 2012; accepted 31 May 2012; published 18 July 2012.

[1] Near-real-time estimates of biomass burning emissions are crucial for air quality monitoring and forecasting. We present here the first near-real-time global biomass burning emission product from geostationary satellites (GBBEP-Geo) produced from satellite-derived fire radiative power (FRP) for individual fire pixels. Specifically, the FRP is retrieved using WF_ABBA V65 (wildfire automated biomass burning algorithm) from a network of multiple geostationary satellites. The network consists of two Geostationary Operational Environmental Satellites (GOES) which are operated by the National Oceanic and Atmospheric Administration, the Meteosat second-generation satellites (Meteosat-09) operated by the European Organisation for the Exploitation of Meteorological Satellites, and the Multifunctional Transport Satellite (MTSAT) operated by the Japan Meteorological Agency. These satellites observe wildfires at an interval of 15–30 min. Because of the impacts from sensor saturation, cloud cover, and background surface, the FRP values are generally not continuously observed. The missing observations are simulated by combining the available instantaneous FRP observations within a day and a set of representative climatological diurnal patterns of FRP for various ecosystems. Finally, the simulated diurnal variation in FRP is applied to quantify biomass combustion and emissions in individual fire pixels with a latency of 1 day. By analyzing global patterns in hourly biomass burning emissions in 2010, we find that peak fire season varied greatly and that annual wildfires burned 1.33×10^{12} kg dry mass, released 1.27×10^{10} kg of PM2.5 (particulate mass for particles with diameter <2.5 μm) and 1.18×10^{11} kg of CO globally (excluding most parts of boreal Asia, the Middle East, and India because of no coverage from geostationary satellites). The biomass burning emissions were mostly released from forest and savanna fires in Africa, South America, and North America. Evaluation of emission result reveals that the GBBEP-Geo estimates are comparable with other FRP-derived estimates in Africa, while the results are generally smaller than most of the other global products that were derived from burned area and fuel loading. However, the daily emissions estimated from GOES FRP over the United States are generally consistent with those modeled from GOES burned area and MODIS (Moderate Resolution Imaging Spectroradiometer) fuel loading, which produces an overall bias of 5.7% and a correlation slope of 0.97 ± 0.2. It is expected that near-real-time hourly emissions from GBBEP-Geo could provide a crucial component for atmospheric and chemical transport modelers to forecast air quality and weather conditions.

Citation: Zhang, X., S. Kondragunta, J. Ram, C. Schmidt, and H.-C. Huang (2012), Near-real-time global biomass burning emissions product from geostationary satellite constellation, *J. Geophys. Res.*, *117*, D14201, doi:10.1029/2012JD017459.

[1]Earth System Science Interdisciplinary Center, University of Maryland, College Park, Maryland, USA.

Corresponding author: X. Zhang, Earth System Science Interdisciplinary Center, University of Maryland, 5825 University Research Ct., College Park, MD 20740-3823, USA. (xiaoyang.zhang@noaa.gov)

0148-0227/12/2012JD017459

[2]Center for Satellite Applications and Research, National Environmental Satellite Data and Information Service, NOAA, College Park, Maryland, USA.
[3]IMSG at Center for Satellite Applications and Research, National Environmental Satellite Data and Information Service, NOAA, College Park, Maryland, USA.
[4]Cooperative Institute for Meteorological Satellite Studies, University of Wisconsin-Madison, Madison, Wisconsin, USA.
[5]IMSG at National Centers for Environmental Prediction, National Weather Service, NOAA, Camp Springs, Maryland, USA.

1. Introduction

[2] Biomass burning emissions deteriorate air quality and impact carbon budgets because of the large amount of aerosols and trace gases released into the atmosphere [*Andreae and Merlet*, 2001; *Langenfelds et al.*, 2002]. For example, global wildfires burn, on average, 3.7 million km^2 of land and release 2013 million tons of carbon emissions per year, which is about 22% of global fossil fuel emissions [*van der Werf et al.*, 2010]. Biomass burning also alters the changes in hydrologic and ecological environments and modifies terrestrial carbon sequestration. Such effects are partially moderated or eliminated with plant regrowth and ecosystem restoration on decadal time scales. However, biomass burning has direct and immediate impacts on air quality and weather conditions which are major environmental risks to human health. Therefore, the availability of information on fires and emissions in near real time for air quality modeling becomes critical.

[3] A large number of research efforts have been devoted to deriving biomass burning emissions using burned area and fuel loading on regional to global scales [e.g., *Seiler and Crutzen*, 1980; *van der Werf et al.*, 2006; *Wiedinmyer et al.*, 2006; *Zhang et al.*, 2008; *Al-Saadi et al.*, 2008; *Urbanski et al.*, 2011]. The first global biomass burning emissions were estimated using statistical and inventory data [*Seiler and Crutzen*, 1980; *Hao et al.*, 1990; *Hao and Liu*, 1994; *Lobert et al.*, 1999; *Galanter et al.*, 2000; *Andreae and Merlet*, 2001]. These data are generally incomplete and only available for specific time periods and the results are of high uncertainty. The availability of global burned area products retrieved from satellite data for specific time periods during past years has improved the estimates of global biomass burning emissions. Particularly, satellite-derived global burned area products include the MODIS (Moderate Resolution Imaging Spectroradiometer) burn scar product [*Roy et al.*, 2002], the MODIS active fire-based burned area [*Giglio et al.*, 2010], the Global Burned Area (GBA) product derived from SPOT/VEGETATION [*Piccolini and Arino*, 2000], and the GLOBSCAR (Global Burn SCARs) burned area produced from the Along Track Scanning Radiometer (ATSR-2) instrument onboard the ESA ERS-2 satellite in 2000 [*Simon et al.*, 2004]. Correspondingly, several data sets of global biomass burning emissions have been established for specific years: (1) monthly emissions at a 0.5° × 0.5° spatial resolution in 2000 from GLOBSCAR, LPJ-DGVM (the Lund-Potsdam-Jena Global Dynamic Vegetation model) and land cover map [*Hoelzemann et al.*, 2004], (2) monthly 0.5° × 0.5° grid emissions in 2000 using burned area from GLOBSCAR and GBA and fuel loading from the terrestrial component of the ISAM (Integrated Science Assessment Model) terrestrial ecosystem mode [*Jain et al.*, 2006], (3) monthly satellite pixel-scale emissions from burned area of GBA-2000 data and global fuel loading maps developed from biomass density data sets for herbaceous and tree-covered land together with global fractional tree and vegetation cover maps [*Ito and Penner*, 2004], (4) the Global Fire Emissions Database (GFED3.1) at a monthly temporal resolution and a 0.5° × 0.5° spatial resolution from 1997 to 2009 using MODIS active fire data and global biogeochemical modeling [*van der Werf et al.*, 2010], (5) daily and 3 hourly global fire emissions disaggregated from monthly GFED3 using MODIS active fires and GOES WF_ABBA fire observations [*Mu et al.*, 2011], and (6) the Fire Inventory from NCAR (FINNv1) produced using daily MODIS hot spots from 2005 to 2010 at a spatial resolution of 1 km and fuel loading assigned to five land cover types [*Wiedinmyer et al.*, 2011]. These results that were derived from different model inputs vary substantially and the quality of emission estimates is difficult to verify. The uncertainty is mainly from the parameters (burned area, fuel loading, factor of combustion, and factor of emission) used for the estimates of biomass burning emissions. For example, burned areas derived from field inventory, satellite-based burn scars, and satellite hot spots differ by a factor of seven in North America and by 2 orders of magnitude across the globe [*Boschetti et al.*, 2004].

[4] Fire radiative power (FRP) has recently emerged as an alternative approach to estimate biomass burning emissions. FRP reflects a combination of the fire strength and size and is related to the rate of biomass burning. Fire radiative energy (FRE) is time-integrated FRP, and is related to the total amount of biomass combusted. Thus, it provides a means to directly measure biomass combustion from satellite data [*Wooster et al.*, 2003]. Satellites observe fires through the radiant component of the total energy released from fires, providing an instantaneous measurement of fire radiance representing FRP—the rate of FRE release [*Kaufman et al.*, 1998; *Wooster et al.*, 2003; *Ichoku and Kaufman*, 2005; *Ichoku et al.*, 2008]. FRP is a proxy for the rate of consumption of biomass and is a function of area being burned, fuel loading, and combustion efficiency. Observed FRP has been successfully used to calculate biomass combusted from wildfires using SEVIRI (Spinning Enhanced Visible and Infrared Imager) radiometer onboard the geostationary Meteosat-8 platform in Africa [*Roberts et al.*, 2005] and MODIS data in both Africa [*Ellicott et al.*, 2009] and globe [*Kaiser et al.*, 2009, 2012].

[5] Quantifying global biomass burning emissions generally rely on fire observations from polar-orbiting satellites. However, their low overpass frequency limits the application of emission estimates for atmospheric and chemical transport models. To serve air quality and weather forecasts, near-real-time emissions with diurnal variation are required in an operational process. To achieve this goal, we establish a system to produce a Global Geostationary Satellite Biomass Burning Emissions Product (GBBEP-Geo) from FRP with a latency of 1 day. The FRP is retrieved using WF_ABBA (wildfire automated biomass burning algorithm) from a network of geostationary satellites consisting of two Geostationary Operation Environmental Satellites (GOES) which are operated by the National Oceanic and Atmospheric Administration (NOAA), the Meteosat second-generation satellites (Meteosat-09) operated by the European Organization for the Exploitation of Meteorological Satellites (EUMETSAT), and the Multi-functional Transport Satellite (MTSAT) operated by the Japan Meteorological Agency (JMA). The GBBEP-Geo results are analyzed spatially and temporally, and evaluated using emission estimates from other products.

2. Methodology

2.1. Modeling Biomass Burning Emissions

[6] Biomass burning emissions are conventionally modeled using four fundamental parameters. These parameters

Table 1. Geostationary Satellites and FRP Detections From WF_ABBA V65

Satellite/Sensor	Spatial Coverage	Spatial Resolution (Nadir)	Observation Frequency
GOES-West and GOES-East Imagers	North America and South America	4 km	30 min
Meteosat-9 SEVIRI	Africa and Europe	3 km	15 min
MTSAT Imager	Asia and Australia	4 km	30 min

are burned area, fuel loading (biomass density), the fraction of biomass combustion, and the factors of emissions for trace gases and aerosols. By integrating these parameters, biomass burning emissions can be estimated using the following formula [*Seiler and Crutzen*, 1980]:

$$E = DM \times F = A \times B \times C \times F. \quad (1)$$

In equation (1), E represents emissions from biomass burning (kg); DM is the dry fuel mass combusted (kg); A is burned area (km^2); B is biomass density (kg/km^2); C is the fraction of biomass consumed during a fire event; and F is the factor of consumed biomass that is released as trace gases and smoke particulates. This simple model has been widely applied to estimate fire emissions in local, regional, and global scales [e.g., *Ito and Penner*, 2004; *Reid et al.*, 2004; *Wiedinmyer et al.*, 2006; *van der Werf et al.*, 2006; *Zhang et al.*, 2008]. The accuracy of the emissions depends strongly on the quality of fuel loading and burned area estimates, which have high uncertainties [e.g., *Zhang et al.*, 2008; *van der Werf et al.*, 2010; *French et al.*, 2011].

[7] Alternatively, *Wooster* [2002] demonstrated a linear relationship between fuel consumption and total emitted fire radiative energy. This is due to the fact that the total amount of energy released per unit mass of dry fuel fully burned is weakly dependent on vegetation types and fuel types, which ranges between 16 and 22 MJ/kg [*Lobert and Warnatz*, 1993; *Whelan*, 1995; *Trollope et al.*, 1996; *Wooster et al.*, 2005]. Thus, biomass burning emission is linearly linked to fire radiative energy in a simple formula [*Wooster*, 2002]:

$$E = DM \times F = FRE \times \beta \times F = \int_{t_1}^{t_2} FRPdt \times \beta \times F, \quad (2)$$

where FRP is fire radiative power (MW); FRE is fire radiative energy (MJ); t_1 and t_2 are the beginning and ending time (second) of a fire event; and β is biomass combustion rate (kg/MJ).

[8] The biomass combustion rate (β) is assumed to be a constant. It is 0.368 ± 0.015 kg/MJ based on field controlled experiments regardless of the land surface conditions [*Wooster et al.*, 2005]. This coefficient has been accepted for the calculation of biomass burning emissions from MODIS FRP and SEVERI FRP [e.g., *Roberts et al.*, 2009; *Ellicott et al.*, 2009], and so this value is also adopted in this study.

[9] An emission factor (F) is a representative value that is used to represent the quantity of a trace gas or aerosol species released into the atmosphere during a wildfire activity. The value is a function of fuel type and is expressed as the number of kilograms of particulate per ton (or metric ton) of material or fuel. This study assigns the emission factor for each emitted species (CO and PM2.5) with land cover type according to values published in literature [e.g., *Andreae and Merlet*, 2001; *Wiedinmyer et al.*, 2006]. Specifically, the emission factors are assigned to five stratified land cover types: 11.07 g/kg (PM2.5) and 77 g/kg (CO) in forests and savannas, 5.6 g/kg (PM2.5) and 84 g/kg (CO) in shrublands, 9.5 g/kg (PM2.5) and 90 g/kg (CO) in grasslands, and 5.7 g/kg (PM2.5) and 70 g/kg (CO) in croplands.

[10] As aforementioned, FRE represents the combination of total burned area and the dry fuel mass combusted (e.g., live foliage, branches, dead leaf litter, and woody materials) in a given time period, which reduces error sources of parameter measurements comparing with the approach employing both burned area and fuel loading in the estimates of biomass burning emissions. Thus, the FRP approach is adopted to produce GBBEP-Geo product, which is described in the following section. The results are evaluated against estimates from equation (1) with good quality data of fuel loading and burned area over the Unite States [*Zhang et al.*, 2008] and against other emission products.

2.2. Fire Radiative Power from Geostationary Satellite Fire Product

[11] Fire radiative power data are retrieved from a set of geostationary satellites. FRP is theoretically a function of fire size and fire temperature. It is empirically related to the difference of brightness temperature between a fire pixel and ambient background pixels at the middle infrared (MIR) wave band of satellites [*Kaufman et al.*, 1998]. Further, FRP is approximated as the difference of MIR spectral radiances between a fire pixel and ambient background pixels in a linear form [*Wooster et al.*, 2003]. The latter approach is adapted by WF_ABBA in the Cooperative Institute for Meteorological Satellite Studies (CIMSS), University of Wisconsin [*Prins et al.*, 1998; *Weaver et al.*, 2004]. Particularly, the WF_ABBA V65 detects instantaneous fires in subpixels using infrared bands around 3.9 and 10.7 μm from a network of geostationary satellite instruments that include SEVIRI on board the Meteosat-9, and Imagers on board both GOES and MTSAT (Table 1). It then derives instantaneous FRP from radiances in single MIR [*Wooster et al.*, 2003]. Further, to minimize false fire detections, the WF_ABBA uses a temporal filter to exclude the fire pixels that are only detected once within the past 12 h [*Schmidt and Prins*, 2003]. Note that this filter may remove early satellite fire observations in an event. The WF_ABBA V65 has been installed in NOAA OSDPD (the Office of Satellite Data Processing and Distribution) to operationally produce FRP from geostationary satellites since late 2009 (http://satepsanone.nesdis.noaa.gov/pub/FIRE/forPo/). The NOAA fire product provides detailed information of WF_ABBA V65 fire detections. It includes the time of fire detection, fire location in latitude and longitude, an instantaneous estimate of FRP, ecosystem type, and a quality flag. The quality flag is defined as flag 0, fire pixel detection with good quality; flag 1, saturated fire pixel; flag 2, cloud-contaminated fire pixel; flag 3, high-probability fire pixel; flag 4, medium-probability fire pixel; and flag 5,

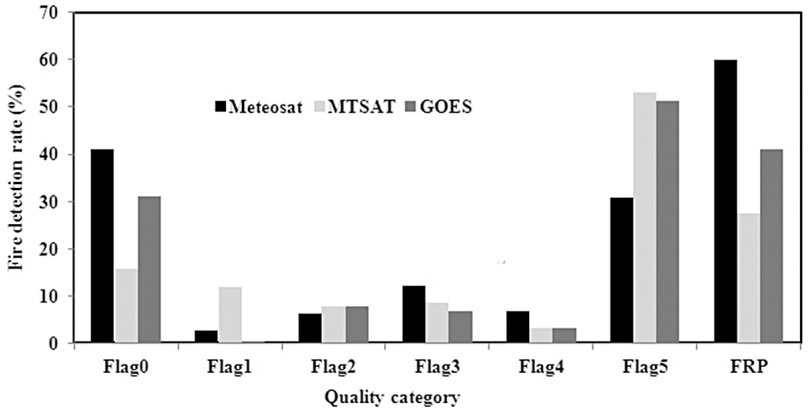

Figure 1. Proportion of fire observations with different quality levels from geostationary satellite data globally in 2010. Flag0, good quality fire pixel; Flag1, saturated fire pixel; Flag2, cloud-contaminated fire pixel; Flag3, high-probability fire pixel; Flag4, medium-probability fire pixel; and Flag5, low-probability fire pixel.

low-probability fire pixel. The ecosystem type in the fire product is based on USGS (U.S. Geological Survey) Global Land Cover Characterization (GLCC) data set which was produced based on 1 km advanced very high resolution radiometer (AVHRR) data spanning April 1992 through March 1993 [*Brown et al.*, 1999]. It consists of 100 different classes. For simplifying analysis in this study, the ecosystem type is reclassified as forests, savannas, shrublands, grasslands, and croplands.

[12] There are two major limitations in the fire data from WF_ABBA V65. First, the fire detection rate with good quality is less than 41%, particularly from MTSAT (Figure 1). Although the FRP is also estimated for fire detections of medium–high probability, the rate of total FRP retrieval is about 60%, 27%, and 41% from Meteosat, MTSAT, and GOES, separately. Second, although geostationary satellites observe the surface every 15–30 min, observations of diurnal fires may, to a great extent, be obstructed by the impact factors including cloud cover, canopy cover, heavy fire smoke, heterogeneity of the surface, large pixel size and view angle of satellites, and weak energy release from fire pixels [*Giglio et al.*, 2003; *Prins and Menzel*, 1992; *Roberts et al.*, 2005; *Zhang et al.*, 2011]. Thus, missing FRP observations cause a great amount of gaps in the spatial and temporal distributions. As a result, FRE in a given time period and region is not able to be directly integrated from satellite-observed FRP. To overcome these limitations, the diurnal patterns of FRP need to be reconstructed, which are described in the following section.

2.3. Simulating Diurnal Pattern of FRP

[13] Diurnal variation in FRP data for each individual fire pixel is simulated using a climatological FRP diurnal pattern. The reconstructed diurnal pattern provides estimates of FRP for a large number of instantaneous fires with both poor detections and nondetections from WF_ABBA V65. To do this, we adopt the approach that was originally developed to reconstruct diurnal pattern of fire size [*Zhang and Kondragunta*, 2008; *Zhang et al.*, 2011]. First, geolocation errors in GOES fire data due to jitter are minimized. Basically, fires observed in two neighboring pixels concurrently are treated as separate fire pixels. However, if fires are semicontinuously observed in one pixel with a neighboring pixel showing sporadic fires within a day, the fires are treated as the same and clustered into one pixel. In other words, a neighboring fire pixel is treated as the same pixel as the given fire pixel if the following conditions are met: (1) the number of instantaneous fire observations in a given fire pixel is larger than that in the neighboring pixel within a day and (2) none of the fire detections in the neighboring pixel is concurrent with those in the given pixel and the observation time of both fire pixels is interspersed. In this way, the number of instantaneous fire detections for the given fire pixel is the total in both pixels. Of course, this simple approach does not necessary provide correct geolocation, but it could improve the estimates of FRE.

[14] Second, both FRP and time (UTC) within a day are recorded for individual fire pixels. If FRP is observed from two satellites within a same half hour for a given pixel, the average value is used. If an instantaneous fire is detected without FRP calculation, only the time is recorded for the determination of fire duration.

[15] Third, FRP diurnal pattern is simulated. The algorithm assumes that the shape of the FRP diurnal pattern is similar in a given ecosystem and that the diurnal pattern of FRP for a given fire pixel can be reconstructed by fitting the climatological diurnal curve corresponding to that ecosystem to the detected fire FRP values. In other words, the magnitude of the reconstructed FRP for an individual fire pixel is generally controlled by the actual FRP observations with good quality although the shape of the diurnal variation can be driven by climatology. Practically, the climatological diurnal pattern at a half-hour interval is generated using the average of FRP values with good quality (flag 0) and with satellite viewing angle less than 40 degree from 2002 to 2005 in North America. The climatological FRP is calculated for forests, savannas, shrubs, grasses, and croplands, separately, after the observation time is converted from UTC to local solar time. These FRP data in a half-hourly interval are then smoothed using Fourier models to remove some spurious values (Figure 2). The climatological diurnal FRP pattern generated from GOES fire data is generally flat, which varies between 160 and 220 MW. This indicates that energy emitted from a fire pixel is similar during a day if a fire occurs. However,

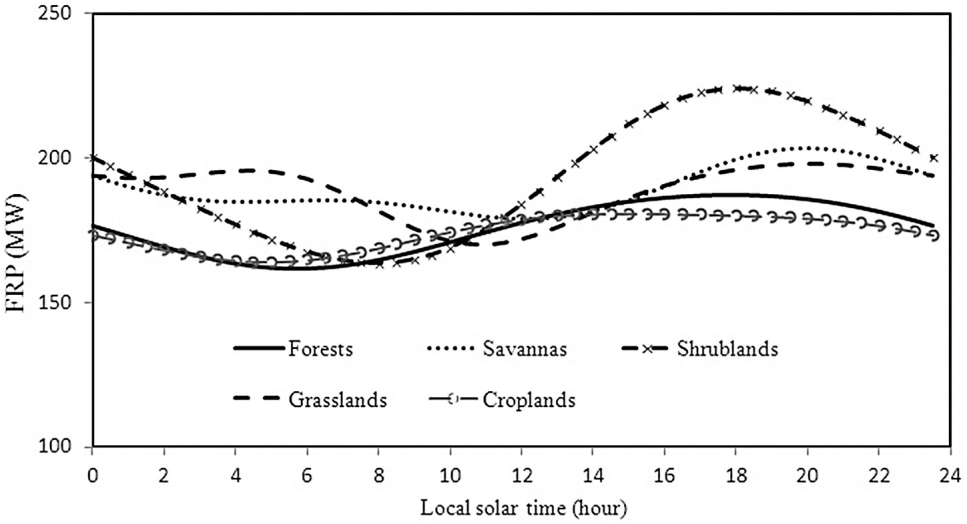

Figure 2. Climatological diurnal FRP (average data from 2002 to 2005) fitted using the discrete Fourier transform model for various ecosystems in North America.

variation is noticeable in the diurnal pattern. FRP increases slightly from morning to late afternoon or evening and decreases gradually during nighttime. The increase of FRP is relatively earlier in forests, shrublands, and croplands while it is later in savanna and grasslands. The magnitude in diurnal variation is largest in shrublands while it is smallest in savannas. This diurnal pattern is likely associated with diurnal variation in fuel moisture, humidity (ambient humidity), and fire weather conditions [*Schroeder and Buck*, 1970; *Rothermel and Mutch*, 1986; *Beck et al.*, 2001; *Cochrane*, 2003; *Giglio*, 2007].

[16] By shifting the climatological diurnal FRP curve for a given ecosystem, the diurnal FRP of an individual fire pixel is reconstructed. The offset of shift is determined from the data pairs of the detected FRP for the given fire pixel and the corresponding values in the climatological curve using a least square method. Because fires in a pixel may not last for a whole day and instantaneous fires are not continuously detected due to the impacts from cloud cover, smoke, low-severity fires releasing limited fire energy, and other factors [*Zhang et al.*, 2011], the fire duration is determined by assuming that fire could be extended 2 hours prior and post instantaneous fire detections if the number of the fire detections (all quality levels) within a day is more than three times. Otherwise, fire occurrences are based on actual satellite detections. Finally, total FRE for a given pixel is the integral of the FRP during the fire period:

$$FRE = \int_{t_s}^{t_e} FRP dt, \tag{3}$$

where t_s is the start time of a fire event and t_e is the end time of the fire pixel.

[17] Because the temporal resolution of geostationary satellites ranges from 15 to 30 min, we set a minimum time step as 30 min (30×60 s). This means that we calculate FRE by assuming that a fire could last for at least a half hour if there is one FRP observation. The half-hourly FRE is binned to calculate hourly biomass burning emissions.

[18] In near-real-time monitoring of biomass burning emissions, we download WF_ABBA V65 fire products automatically from NOAA public ftp site (ftp://140.90.213.161/FIRE/forPo/). The diurnal pattern of FRP is then simulated for the previous day (UTC time) based on fire observations globally for estimating fire emissions. As a result, the GBBEP-Geo is produced with a latency of 1 day across the globe.

[19] The applicability of near-real-time estimates in GBBEP-Geo is demonstrated by analyzing global biomass burning emissions in 2010. Because pixel size varies across the globe, the emissions in the individual fire pixels are resampled to a spatial resolution of 0.25° grid for the investigation of spatial pattern. Diurnal patterns in hourly emissions are aggregated in local solar time from various regions. Daily and monthly emissions are the sum of hourly values for a given region and an ecosystem type, separately. Peak fire season in a 0.25° grid is calculated by determining the middle day within a moving 30 day window where maximum 30 day emission occurs during a year. This way can provide natural fire calendar instead of human-defined month calendar.

2.4. Assessment of the Estimates of Global Biomass Burning Emissions

[20] Global estimates of emissions from wildfires are compared with other models because of the lack of ground truth data. We evaluate the FRE-based GBBEP-Geo with the NOAA GOES Biomass Burning Emission Product (GBBEP), the NASA Quick Fire Emission Data set (QFED), GOES-R (next generation GOES) fire proxy data, and Global Fire Emissions Database (GFED) version 3.1. NOAA GBBEP uses the conventional fire emission model (equation (1)) developed by *Seiler and Crutzen* [1980] and the improved parameterizations to estimate hourly biomass burning emissions across Contiguous United States (CONUS) [*Zhang et al.*, 2008]. In GBBEP product, fuel loading is obtained from the MODIS Vegetation Property-based Fuel System (MVPFS) which was developed from MODIS percent vegetation cover, leaf area index, and land cover type data at a spatial resolution of 1 km [*Zhang and*

Kondragunta, 2006]. Fuel combustion efficiency and emission factor vary with fuel moisture condition [*Anderson et al.*, 2004], where the weekly fuel moisture category was retrieved from AVHRR data [*Zhang et al.*, 2008]. Burned area was simulated using half-hourly fire sizes obtained from the GOES-East WF_ABBA fire product [*Zhang et al.*, 2008]. We obtain GBBEP PM2.5 in 2010 from NOAA public ftp site (ftp://satepsanone.nesdis.noaa.gov/EPA/GBBEP/) to evaluate our FPR-based GBBEP-Geo results. Note that GBBEP only uses GOES-East fire detections in emission estimates over CONUS while GBBEP-Geo combines GOES-East and GOES-West fire data. To make an appropriate comparison, we remove fire detections from GOES-W in GBBEP-Geo and only select the emission estimates from GOES-East.

[21] We also compare our GBBEP-Geo with Quick Fire Emission Data set Version 1 (QFED v1, http://geos5.org/wiki/index.php?title=Quick_Fire_Emission_Dataset_%28QFED%29). QFEDv1, the near-real-time biomass burning emission system from the NASA Global Modeling and Assimilation Office, produces daily total of black and organic carbon at a spatial resolution of 0.25 × 0.3125 degrees, which is derived using MODIS fire count and FRP products from both Aqua and Terra satellites. Similar to the approach developed by *Kaiser et al.* [2009], cloud effects on FRP observations are reduced using the proportion of cloud cover. Terra MODIS FRP and Aqua MODIS FRP are then calibrated against Global Fire Emissions Data version 2 (GFED2) [*van der Werf et al.*, 2006], separately. This method accounts for the differences in the fire strengths at the local time of the satellite overpass and ensures redundancy in case one of the satellites fails. For the comparison with QFEDv1, the total value of both black and organic carbon is converted from dry mass in GBBEP-Geo using a coefficient of 0.009 [*Chin et al.*, 2007].

[22] The third data set used to assess the WF_ABBA FRP-based biomass burning emissions is the GOES-R fire proxy simulated at CIRA (Cooperative Institute for Research in the Atmosphere), Colorado State University. This proxy simulates 4 GOES-R ABI (Advanced Baseline Imager) bands (2.25 μm, 3.9 μm, 10.35 μm, and 11.2 μm) that include fire hot spots using a high-resolution Regional Atmospheric Modeling System (RAMS) model [*Grasso et al.*, 2008; *Hillger et al.*, 2009]. The artificial fires were laid out in a regular grid size of 400 m and a temporal resolution of 5 min. Fire temperature that was artificially set spatially varied from 400°K to 1200°K in 100°K intervals. Fires were set to vary temporally and weather conditions also changes. These fire hot spots, which lasted 6 h, were simulated for 4 different fire events which were detected by MODIS data on 23 October 2007, California, 26 October 2007, California, 5 November 2008, Arkansas, 24 April 2004, Central America. Fire temperature at the 400 m grids was used to calculate FRP. These simulated FRP values calculated from fire temperature and fire grid size were also taken as the ground "truth" for evaluation our global biomass emission algorithm.

[23] The GOES-R ABI imagery at an approximately 2 × 2 km resolution was simulated using the anticipated point spread function from the 400 m fires [*Grasso et al.*, 2008; *Hillger et al.*, 2009; *Schmidt et al.*, 2010]. Based on these simulated instantaneous radiance, the WF_ABBA was used to process the detection of fire characteristics. In the WF_ABBA output, fires may not always be detected and the fire characteristics may not be provided because of weak fire emission, saturation, and cloud impacts. Fire detection rate is larger than 84% for fire pixel with FRP > 75 MW while very small fires are not detectable. The WF_ABBA FRP is then used to estimate diurnal FRP variation and PM2.5 emissions using the GBBEP-Geo algorithm. The results are compared with simulated ground "truth" after the data pairs are aggregated to a temporal resolution of 1 hour. Because the factors of converting FRE to biomass burning emissions in current algorithm are constant for a give fire event, the FRE difference between proxy data and the estimates from GBBEP-Geo algorithm represents the quality of biomass burning emission estimates.

[24] The fourth data set is GFED3.1. GFED3.1 provides monthly biomass burning emissions from 1997 to 2010 at a spatial resolution of 0.5° using burned area and fuel loading [*van der Werf et al.*, 2010]. Basically, biomass burning emissions were produced from a biogeochemical model which employed monthly MODIS burned area and active fires, land cover characteristics, and plant productivity [*van der Werf et al.*, 2010]. We obtain GFED3.1 data in 2010 from a website (http://www.falw.vu/~gwerf/GFED/GFED3/emissions/). Monthly DM data are calculated from three regions for comparing with GBBEP-Geo estimates, which are South America, North America, and Africa.

3. Results

3.1. Spatial Pattern in Annual Global Biomass Burning Emissions

[25] Global wildfires release trace gases and aerosol with a great spatial variability at both the fire pixel and the geographical grid of 0.25° scales. Figure 3 shows the spatial pattern in annual biomass burning emissions for dry mass combustion, PM2.5 emissions, and CO emissions. The biomass burning emissions are large in South America and Africa while the values are relatively small in Europe and Asia. In most parts of southern Brazil and Bolivia in South America, dry mass combusted per grid cell is more than 1.0×10^8 kg and emissions released per grid cell are more than 1.0×10^6 kg of PM2.5 and 1.0×10^7 kg of CO. Similarly, large emissions in Africa occurred in Angola, Zambia, Botswana, Zimbabwe, Zaire, Rwanda, Burundi, and southern Sudan. The largest biomass burning appeared in the boundary between northern Rwanda and eastern Zaire, where fires consumed 4.3×10^9 kg of DM, and emitted 4.8×10^7 kg of PM2.5 and 4.2×10^8 kg of CO in a 0.25° grid. However, emissions are not estimated for most of the regions in India, the Middle East, and boreal Asia (including Siberia) because of the lack of coverage from the multiple geostationary satellites.

[26] Biomass burning emissions vary greatly by continent and ecosystem. Forest fires dominated in North America (region A), South America (region B), and Eastern Asia (region E), which burned forest dry mass of 7.17×10^{10} kg, 1.50×10^{11} kg, and 6.17×10^{10} kg in 2010, separately (Figure 3 and Table 2). It accounts for 43.6%, 40.7% and 39.5% of total dry mass burned in these corresponding regions. In contrast, savanna fires burned 4.52×10^{11} kg and 1.45×10^{10} kg of dry mass in Africa and Australia, separately, which accounts for 76.5% and 75.8% of total dry mass burned across these regions. In Europe and Western Asia (region D), the amount of dry mass burned is similar for

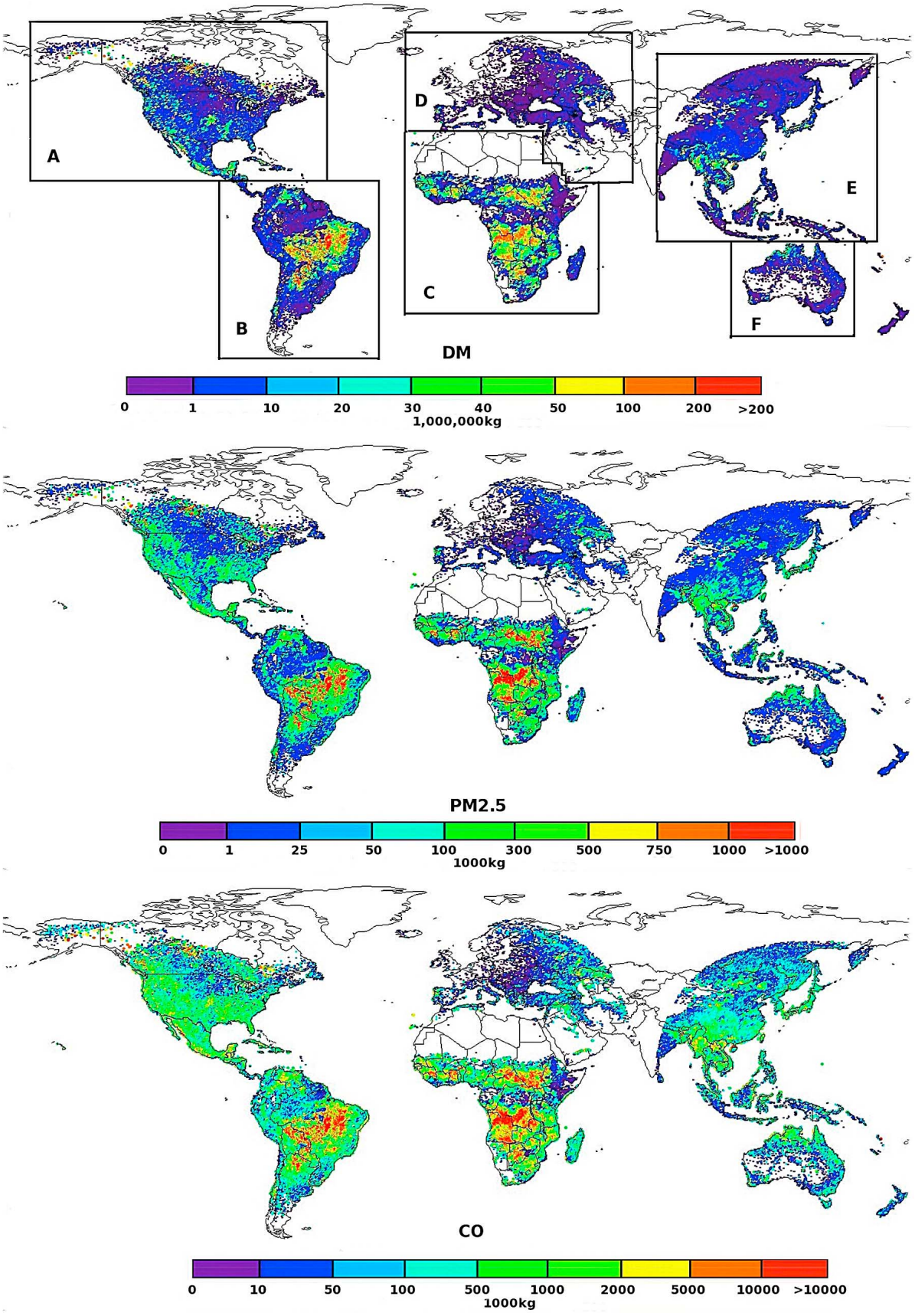
A
B
C
D
E
F
DM
0 1 10 20 30 40 50 100 200 >200
1,000,000kg
PM2.5
0 1 25 50 100 300 500 750 1000 >1000
1000kg
CO
0 10 50 100 500 1000 2000 5000 10000 >10000
1000kg

Figure 3

Table 2. Dry Mass (10^9 kg) Consumed in Different Regions and Ecosystems[a]

	Forests	Savannas	Shrublands	Grasslands	Croplands	Total
North America (A)	71.67	18.89	46.35	8.20	19.17	164.28
South America (B)	150.3	105.3	22.16	72.44	19.28	369.48
Africa (C)	43.96	452.2	40.91	9.43	44.71	591.22
Europe and West Asia (D)	6.59	2.77	3.14	7.54	6.16	26.21
Eastern Asia (E)	61.68	10.06	16.45	32.59	35.24	156.02
Australia (F)	0.752	14.523	3.487	0.005	0.521	19.288
Total	334.952	603.743	132.497	130.205	125.081	1326.5

[a]The region labels are described in Figure 3.

forests, grasslands, and croplands. Globally, dry mass was mostly consumed by savanna fires (47.8%), followed by forest fires (23.5%), shrubland fires (10.1%), cropland fires (9.0%), and grassland fires (9.7%). This pattern is mainly due to the large dry mass combustion in Africa (44.6%) and South America (27.8%).

[27] The spatial pattern and the relative proportion of emissions in trace gases and aerosols are similar to that of dry mass consumed (Tables 3 and 4). PM2.5 emissions are 6.1×10^9 kg in Africa, 3.4×10^9 kg in South America, 1.4×10^9 kg in Eastern Asia, and 1.4×10^9 kg North America. Similarly, CO emitted is 55.6×10^9 kg and 31.2×10^9 kg in Africa and South America, separately. Patterns of fire emissions by ecosystem type match the patterns of dry biomass consumed.

3.2. Seasonal Pattern in Global Biomass Burning Emissions

[28] The magnitude of biomass burning emissions also presents distinctively seasonal variation. The seasonal emissions are shown using monthly global PM2.5 emissions (Figure 4). In North America, the maximum monthly PM2.5 emissions are 3.27×10^8 kg in June and 3.35×10^8 kg in July, which are mainly associated with fires in western North America. In South America, the values are 1.35×10^9 kg in August and 0.62×10^9 kg in September, which accounts for about 60% of annual emissions. These large emissions are mostly from fires in Brazil and Bolivia. In Africa, large monthly PM2.5 emissions are 7.89×10^7 kg (12.9%) in December, 8.53×10^8 kg (13.9%) in January, 8.03×10^8 kg (13.1%) in July, 1.05×10^9 kg (17.2%) in August, and 7.51×10^8 kg (12.3%) in September. Large emissions in December and the following January are from Sahelian and sub-Sahelian region while emissions during July–September are associated with fires in southern Africa. This difference results in seasonal emissions across Africa showing two distinct peaks. In Europe and west Asia (region D), monthly emissions are 2.14×10^8 kg (16.1%) in March, 1.38×10^8 kg (10.3%) in April, 1.63×10^8 kg (12.2%) in August, and 1.37×10^8 kg (10.2%) in September. The two peaks are likely related to agricultural fires. In eastern Asia (regions E) and Australia (F), the largest monthly emissions appear in June, July, and August.

[29] Figure 5 presents detailed variation in daily emission across various regions. On average, the daily PM2.5 value is $3.78 \times 10^6 \pm 4.35 \times 10^6$ kg in North America, $0.94 \times 10^7 \pm 1.39 \times 10^7$ kg in South America, $1.68 \times 10^7 \pm 1.22 \times 10^7$ kg in Africa, $3.70 \times 10^6 \pm 2.43 \times 10^6$ kg in Europe and west Asia (Region D), $6.33 \times 10^5 \pm 1.09 \times 10^6$ kg in eastern Asia, and $6.49 \times 10^5 \pm 5.32 \times 10^5$ kg in Australia. PM2.5 emissions in South America increase rapidly from late July, reach the peak in late August with a daily value as large as 4.35×10^7 kg, and decrease in late October. In Africa, the emission season is long, ranging from late May to late October and from December to February with the daily emission value varying from about 3.0×10^7 kg to 6.23×10^7 kg. In North America, it ranges from May to September with a peak occurring in late July. The daily peak emission value is 2.23×10^7 kg. Similarly, fire emissions in Asia (Region E) present a peak in boreal summer with a daily value less than 4.6×10^6 kg except for 2 days. In contrast, the seasonality of fire emissions in Australia is not distinguishable and daily emissions are generally less than 2.0×10^6 kg.

[30] Figure 6 shows spatial pattern in the timing of peak fire season occurrence. Although the timing is very complex on a 0.25° grid, the general pattern is evident. In the agricultural regions over center North America, the timing of peak emissions occurs during April–May, which is associated with preplanting periods for fertilizing the soil. Peak emission timing is during July–August in western North America because of hot temperature and dry conditions, during April–May in Florida because of limited precipitation, during August–September in northern eastern Asia. In Europe and west Asia, occurrence of peak emission timing dominates during April–June (agricultural fires according to ecosystem types) and in July–August (wildfires). Across the northern tropical savanna climate region (0°–20°N), the peak emission occurs during November to the following March. This pattern matches very well to the dry season period [*Zhang et al.*, 2005]. For example, peak emission presents a gradient in the Sahelian and sub-Sahelian region, which varies from late September in north to the following middle March in southern area. In southern Africa, the peak emission timing varies from late June in northwest to early October in southeast. In South America, peak fire season occurs in January–February in north Andes and August–September in Amazon Basin. The peak emission timing shifts from August to the following January from southwest to northeast of Brazilian Shield. Although fires are limited in Argentina and Chile, the peak appears in January–March.

Figure 3. Estimates of global biomass burning emissions in a geographical grid of 0.25° for 2010. (top) Annual dry mass combusted, (middle) PM2.5 emissions, and (bottom) CO emissions. The regions labeled with A, B, C, D, E, and F are used for further regional analysis and discussion. Note that there is no coverage in parts of high latitudes, the Middle East, and India.

Table 3. PM2.5 Emissions (10^9 kg) in Different Regions and Ecosystems[a]

	Forests	Savannas	Shrublands	Grasslands	Croplands	Total
North America (A)	0.714	0.188	0.281	0.070	0.099	1.352
South America (B)	1.50	1.05	0.134	0.621	0.099	3.404
Africa (C)	0.487	5.006	0.274	0.090	0.255	6.112
Europe and West Asia (D)	0.073	0.031	0.021	0.072	0.035	0.232
East Asia (E)	0.683	0.111	0.110	0.310	0.201	1.415
Australia (F)	0.008	0.161	0.023	0.00004	0.003	0.196
Total	3.465	6.547	0.843	1.163	0.692	12.711

[a]The region labels are described in Figure 3.

3.3. Diurnal Variation in Biomass Burning Emissions

[31] Distinct diurnal patterns in hourly biomass burning emissions vary by region (Figure 7). PM2.5 emissions are mainly released from fires during 8:00–18:00 local solar time (LST) accounting for 80% of the daily emissions. In Africa, the diurnal pattern exhibits a normal distribution. The peak hour occurs around 13:00 with a maximum value of 15% of the daily total emissions. A similar diurnal pattern appears in North America with a peak hourly value of 11%. In contrast, the hourly emissions show a hat shape with a peak hourly value of about 11% in South America and Asia and Australia, separately. The largest hourly emission occurs earlier in the day in Asia and Australia while it does later in South America. The flat peak is associated with the peak shifts with land cover types [*Giglio*, 2007; *Zhang and Kondragunta*, 2008]. In South America, the peak shifts about 1.5 hours among different land cover types. Moreover, the proportion of emissions in grasslands from 11:00 to 15:00 is very similar, which results in a flat peak. It is likely that herbaceous vegetation provides finer and lighter fuels that dry out quickly, which could result in fire ignitions at any time of the day [*Giglio*, 2007]. The shift in the diurnal cycle is also likely influenced by fire spread rates affected by synoptic-scale meteorological events and weather conditions [*French et al.*, 2011; *Beck and Trevitt*, 1989].

[32] Overall, the result of diurnal pattern is comparable with previous reports [*Roberts et al.*, 2005, 2009; *Giglio*, 2007; *Justice et al.*, 2002; *Zhang and Kondragunta*, 2008; *Mu et al.*, 2011]. Note that the diurnal pattern of total PM2.5 emissions is generally controlled by the number of actual fire occurrences, which is different from the climatological diurnal pattern of individual FRP values. The latter is referred to as the mean FRP value in a given half hour if a fire is to occur.

3.4. Comparisons of GBBEP-Geo With Other Estimates

[33] Figure 8 presents the PM2.5 comparison between GBBEP-Geo estimates from FRP and GBBEP product calculated from burned area and fuel loading. The daily emission values over CONUS are basically distributed along a 1:1 line although there are a few outliers. The correlation between these two estimates is statistically significant ($P < 0.0001$). The root-mean-square error (RMSE) in daily emissions is 4.99×10^5 kg for all of the samples. The linear regression (at 95% confidence) slope is 0.968 ± 0.019 ($P < 0.00001$), which indicates that there is no obvious biases. The determination of correlation (R^2) reveals that the GBBEP-Geo explains 88% of the variation in GBBEP. The difference in annual emissions shows that GBBEP-Geo is 5.7% larger than GBBEP. This result indicates that the FRP-based emission amount is overall equivalent to the estimates from the burned area and fuel loading approach. Because the fire sources in these two estimates are all from GOES-East, they have the same omission and commission errors in fire detections. In other words, this comparison is not necessary to validate the absolute magnitude of biomass burning emissions from GBBEP-Geo. Instead, it demonstrates that the FRP (or FRE) is an effective proxy to replace burned area and fuel loading for the estimates of biomass burning emissions from wildfires.

[34] Emission estimates from geostationary satellites are also evaluated by comparing with the total emissions of both black and organic carbon from QFEDv1 in Africa and South America (Figure 9). In Africa (around 25°S–5°N), the monthly emission value is similar in both data sets although GBBEP-Geo emissions are about 5%, 1%, and 13% larger than QFEDv1 emissions in July, August, and September, separately. In contrast, the monthly QFEDv1 emission in South America (around 35°S–10°N) is about 54%, 75%, and 87% of GBBEP-Geo value in July, August, and September, separately. Overall, their values during these 3 months are comparable with a ratio (GBBEP-Geo/QFED) of 1.3 and 1.1 in South America and Africa. This means that these two estimates are strongly comparable, particularly in Africa.

[35] Figure 10 shows the FRE comparison between ground "truth" of the simulated GOES-R fire proxy data and estimates derived from GBBEP-Geo algorithm. The results indicate that FRE values are well estimated for small/weak

Table 4. CO Emissions (10^9 kg) in Different Regions and Ecosystems[a]

	Forests	Savannas	Shrublands	Grasslands	Croplands	Total
North America (A)	6.266	1.652	3.59	0.665	1.211	13.384
South America (B)	13.15	9.217	1.717	5.88	1.219	31.185
Africa (C)	4.265	43.864	3.518	0.849	3.129	55.624
Europe and West Asia (D)	0.639	0.269	0.271	0.679	0.432	2.289
East Asia (E)	5.983	0.976	1.414	2.933	2.467	13.773
Australia (F)	0.073	1.409	0.300	0.0004	0.036	1.819
Total	30.378	57.387	10.81	11.006	8.494	118.074

[a]The region labels are described in Figure 3.

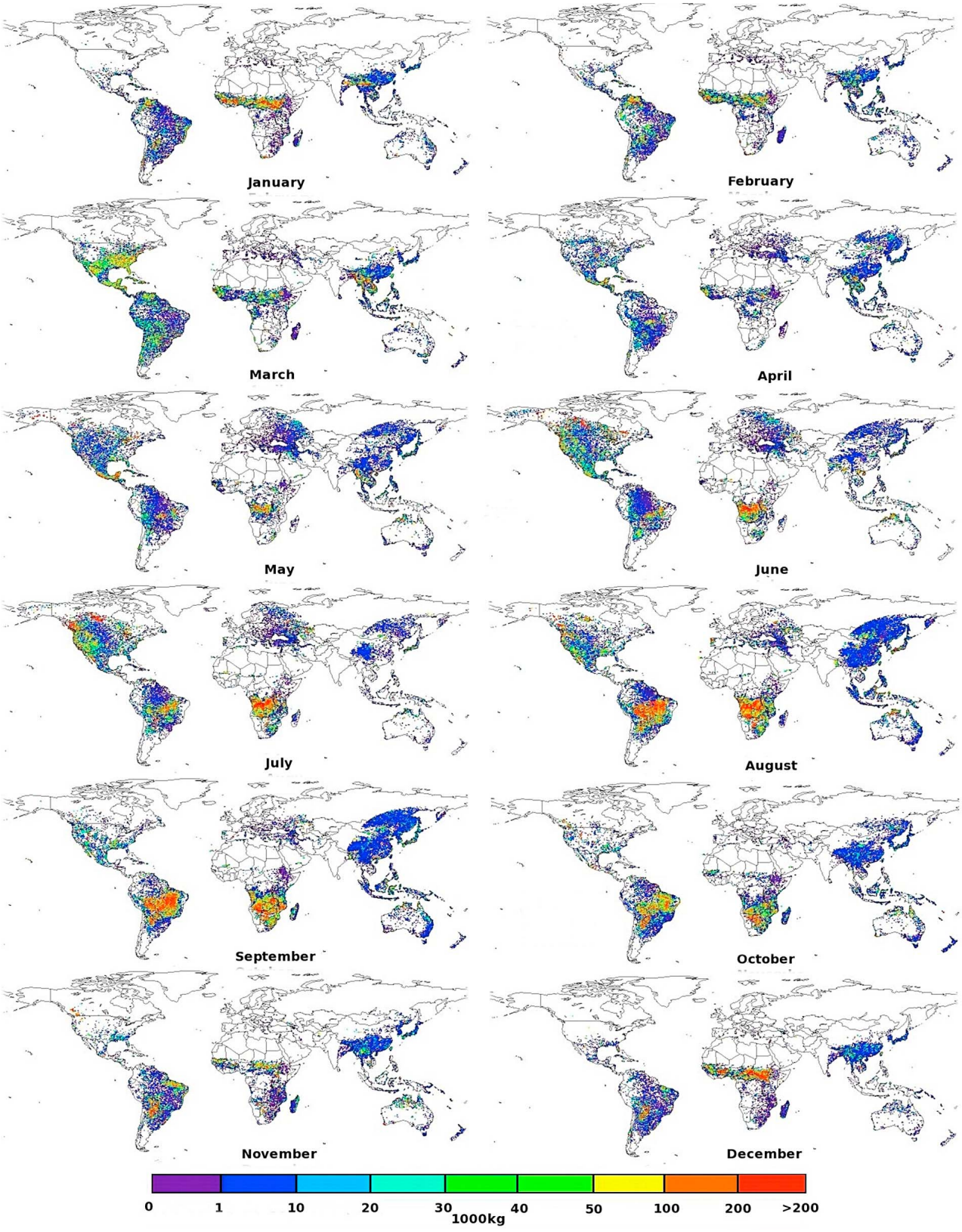

Figure 4. Monthly PM2.5 burning emissions aggregated in a 0.25° grid across the globe in 2010. Note that there is no coverage in parts of high latitudes, the Middle East, and India.

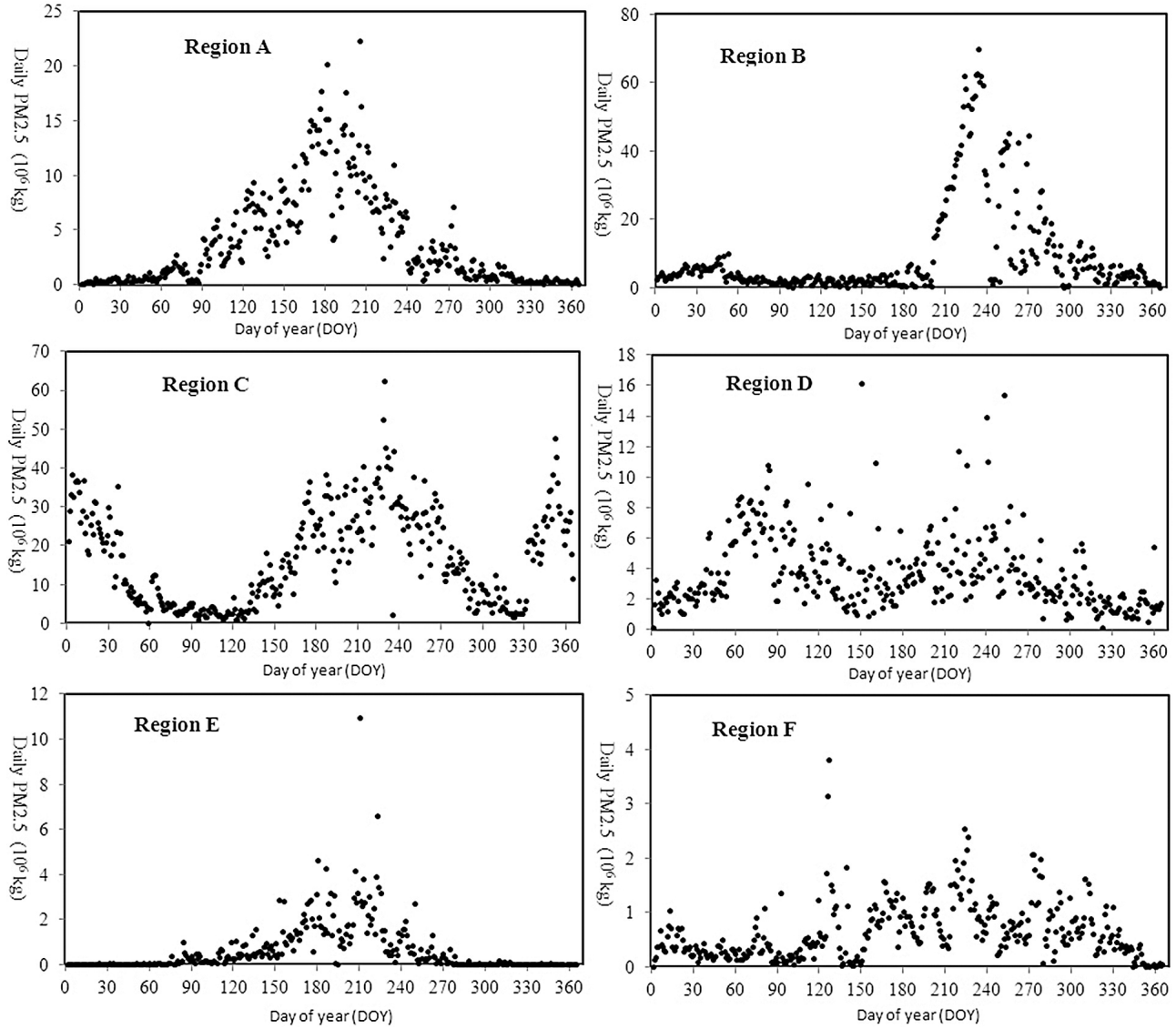

Figure 5. Daily PM2.5 emissions estimated from multiple geostationary satellites over the six regions in 2010.

fires while the values are underestimated for large/strong fires. Overall the hourly mean FRE estimated accounts for 90% of the variation in the "truth." As a whole of the four fire events, the total FRE estimated from the GBBEP-Geo is 12.4% smaller than "truth." This FRE difference represents the quality of biomass burning emissions because the factor used to convert FRE to emissions in current algorithm is constant.

[36] Figure 11 indicates that monthly DM in GBBEP-Geo is significantly correlated with GFED3.1 estimate in Africa (R^2 = 0.89), in South America (R^2 = 0.88), and in North America (R^2 = 0.85). However, the magnitude is discrepant. In African, monthly GBBEP-Geo DM is consistently smaller than GFEDv3.1 estimate with a factor larger than 2, which leads to a factor of 3.4 in annual DM. In South America, GBBEP-Geo DM is smaller than GFEDv3.1 DM from May to October while it is larger during other months. Because the emission estimates differ greatly in the fire peak season (August and September) in 2010, which accounts for 85% of annual emissions in GFEDv3.1 and 57% in GBBEP-Geo, the annual DM in GBBEP-Geo is smaller than GFEDv3.1 estimate with a factor of 3.8. In North America, GBBEP-Geo DM is slightly smaller than GFEDv3.1 estimate with a factor of 1.36, which is mainly due to the large difference in June and July. In contrast, DM is larger in GBBEP-Geo than in GFEDv3.1 with a factor of 2.1 in the region of temperate North America and Central America. Similarly, GFED generally produces relatively lower fire emissions in this region comparing with other studies [*Al-Saadi et al.*, 2008; *Kaiser et al.*, 2012].

4. Discussion

[37] The high frequency of fire observations from multiple geostationary satellites enables us to estimate global biomass burning emissions in near real time. The operational product of GBBEP-Geo could meet the needs to provide hourly emissions in near real time from individual fire pixels for air

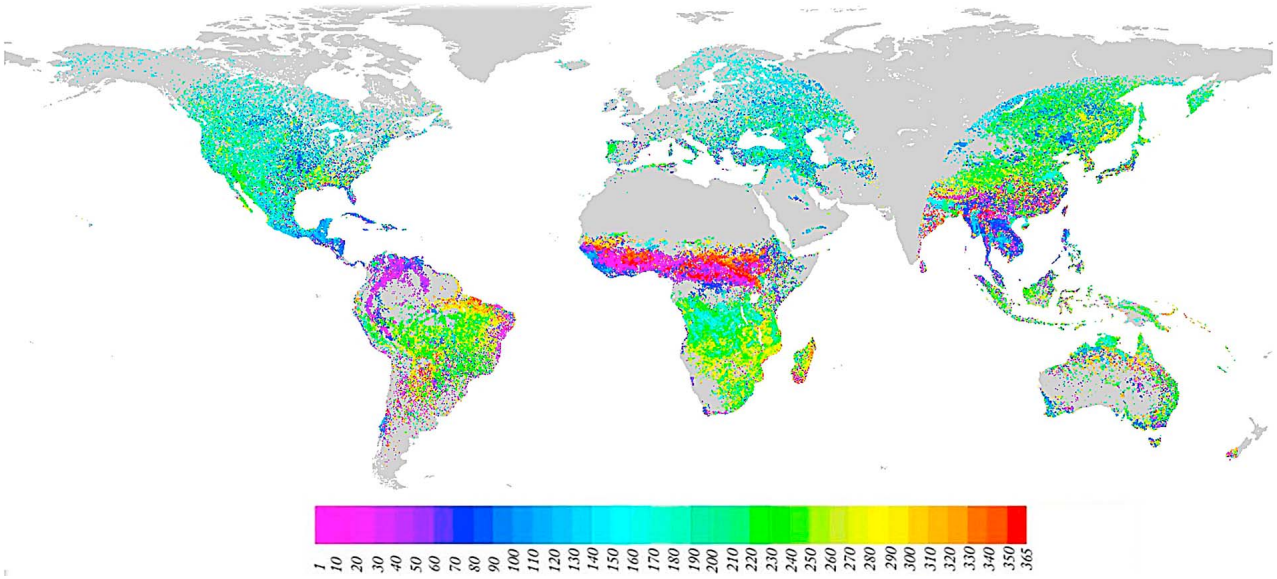

Figure 6. Occurrence of peak time in biomass burning emissions in a 0.25° grid in 2010. The time represents the middle day of a 30 day window with maximum emissions in a year. The color legend refers to the day of year (DOY).

quality and weather forecasts because fire emissions are one of the critical inputs into the atmospheric and chemical transport models [*Yang et al.*, 2011]. Estimates of biomass burning emissions from diurnal geostationary FRP observations in GBBEP-Geo greatly simplify conventional model parameters of burned area and fuel loading. The applicability of GBBEP-Geo is demonstrated by comparing with NOAA GBBEP, QFEDv1 estimates, and GOES-R fire proxy although the uncertainty of emission estimates has yet to be fully evaluated because reliable in situ data are scarcely available.

[38] Comparing GBBEP-Geo data set with the available literature values further improves our understanding of the challenging in the qualification of fire emissions. The GBBEP-Geo estimates are generally small compared to previous studies of global wildfire emissions that are calculated monthly at a spatial resolution of 0.5° using burned area, fuel loading and combustion factors [*Jain et al.*, 2006; *Ito and Penner*, 2004; *Hoelzemann et al.*, 2004; *van der Werf et al.*, 2010] (Table 5). In GBBEP-Geo estimates, global DM (excluding most parts of boreal Asia, the Middle East, and India) is 1.326×10^{12} kg in 2010. In the region without geostationary satellite coverage, wildfires are mainly located in boreal Asia, which burned about 2.56×10^{11} kg DM on average from 1997 to 2009 [*van der Werf et al.*, 2010]. If excluding these fire emissions and assuming that the fire

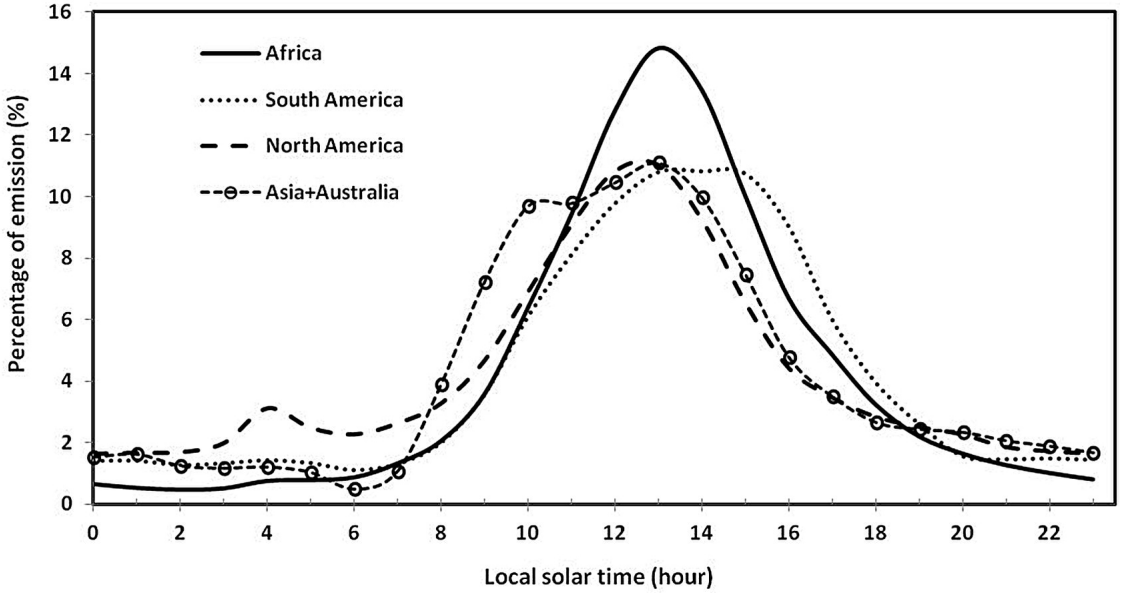

Figure 7. Diurnal variability in the PM2.5 emissions derived from multiple geostationary satellites.

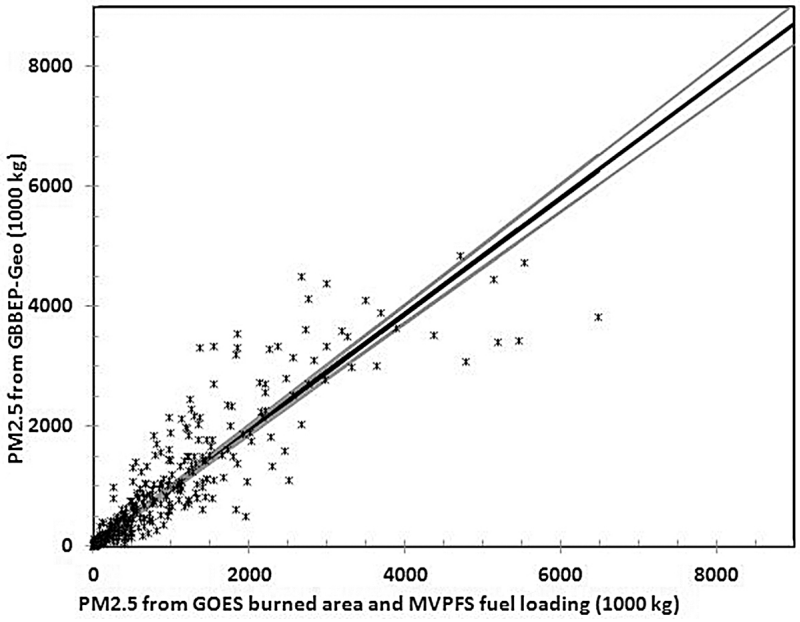

Figure 8. Scatterplot of the GBBEP-Geo FRP-based PM2.5 against NOAA GBBEP daily emissions derived from burned area and fuel loading over CONUS in 2010. The dark line is the ordinary least squares linear best fit passing through the origin and the gray lines are the 95% confidence intervals on the mean.

activities in 2010 would be to some content comparable to those in previous years, GBBEP-Geo estimate turns out to be about 2–3 times smaller than other estimates [*Jain et al.*, 2006; *Ito and Penner*, 2004; *Hoelzemann et al.*, 2004, *van der Werf et al.*, 2010] (Table 5). Most of the difference comes from the emission estimates in Africa, where the GBBEP-Geo estimate is 3.4 times less than those from GFED3.1 in 2010. In contrast, the differences are relatively small in other regions. This magnitude of difference is also true when comparing of GBBEP-Geo PM2.5 emissions with others [e.g., *Wiedinmyer et al.*, 2011].

[39] GBBEP-Geo estimates, however, present a similar magnitude of emission estimates to other FRP-based approaches (Table 5). Using SEVERI FRP, *Roberts et al.* [2009] obtained a fuel consumption of 8.55×10^{11} kg (DM) in Africa between February 2004 and January 2005, which is about 2.3 times smaller than that from GFEDv3.1 [*van der Werf et al.*, 2010]. Based on MODIS FRP, *Ellicott et al.* [2009] calculated an average of 7.16×10^{11} kg DM burned per year between 2001 and 2007 in Africa, which is 3.5 times less than GFEDv2 [*van der Werf et al.*, 2006] and 3.0 times less than GFEDv3.1 [*van der Werf et al.*, 2010].

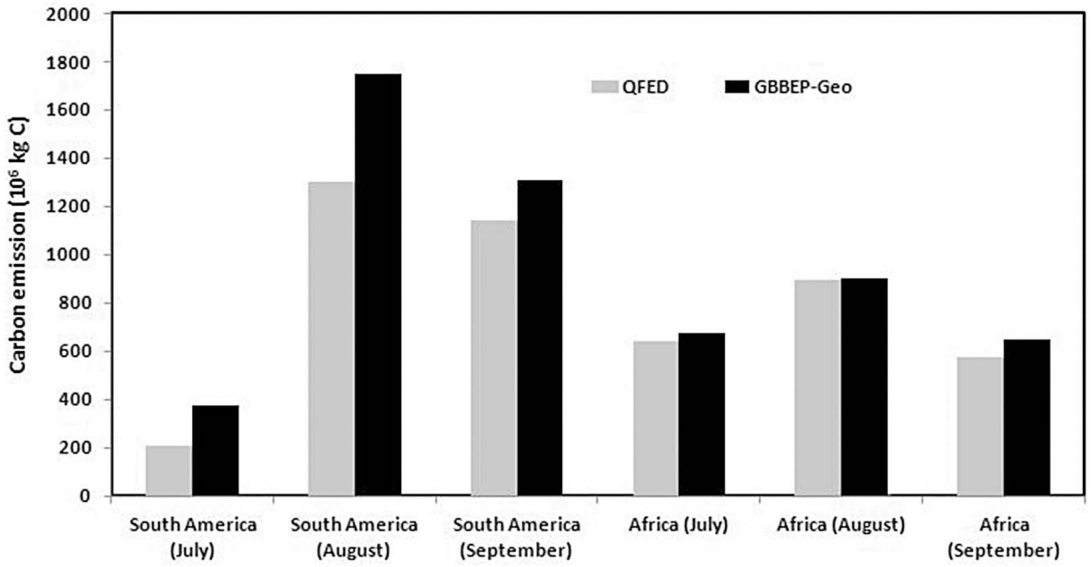

Figure 9. Comparison of monthly black and organic carbon estimated from GBBEP-Geo and QFED in Africa and South America, separately.

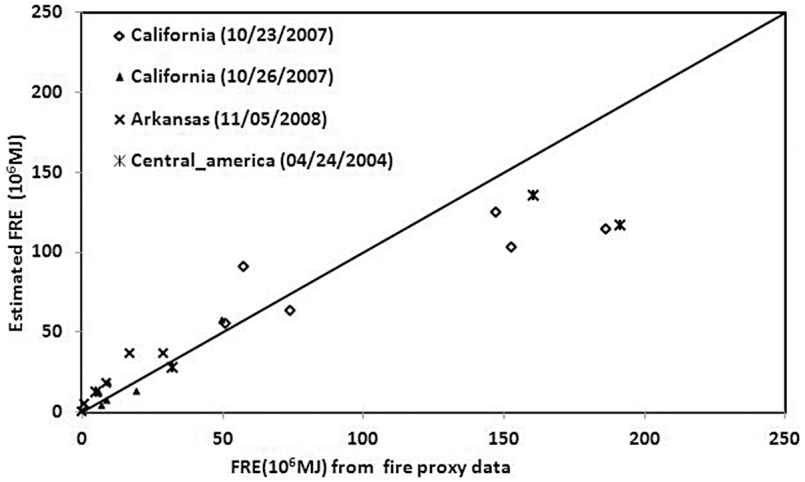

Figure 10. Comparison of hourly FRE calculated from WF_ABBA detected from the fire proxy radiance with fire proxy FRE in the four proxy fire events.

[40] The modeled results using the *Seiler and Crutzen* [1980] equation are largely dependent on the input quality of burned area, fuel loading, and combustion factors [e.g., *van der Werf et al.*, 2010; *Hoelzemann et al.*, 2004]. Although global burned area has been greatly improved with the development of high-resolution satellite data from 500 m to 1 km [*Roy et al.*, 2008; *Plummer et al.*, 2006; *Tansey et al.*, 2008; *Giglio et al.*, 2009], the discrepancy among various satellite-based global products is still very large [*Giglio et al.*, 2010; *Roy and Boschetti*, 2009; *van der Werf et al.*, 2010; *Conard et al.*, 2002; *Boschetti et al.*, 2004]. The difference could be as large as from 2 to 10 times in some regions because of the impacts from unburned patches in a fire pixel and persistent cloud and smoke [*Conard et al.*, 2002; *Boschetti et al.*, 2004]. Global fuel loading is generally derived from land cover types and biomass density data [*Ito and Penner*, 2004; *Jain et al.*, 2006; *Wiedinmyer et al.*, 2011], global vegetation model [*Hoelzemann et al.*, 2004], and global biogeochemical models [*van der Werf et al.*, 2006]. The related uncertainty could result in a discrepancy of as large as 4 times [*Campbell et al.*, 2007]. Combustion factor depends on fuel type and burn severity. The combustion factor for forest wood is about 0.3–0.5 in most models [e.g., *Ito and Penner*, 2004; *Soja et al.*, 2004; *Wiedinmyer*

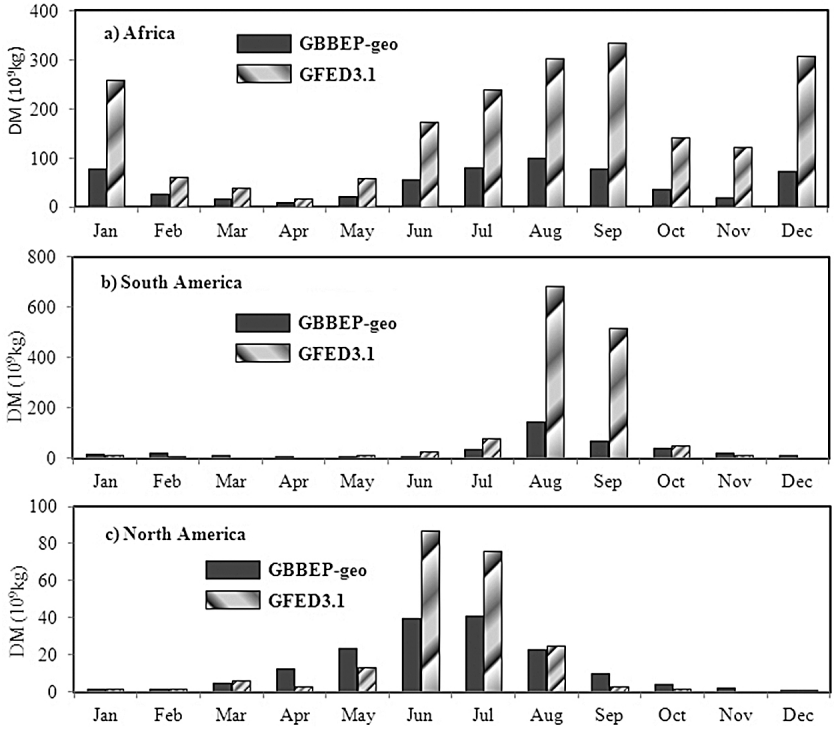

Figure 11. Comparison of DM between GFED3.1 and GBBEP-Geo estimates in 2010.

Table 5. Comparisons of Annual Dry Mass Combustion (10^9 kg) From Various Studies[a]

Methods	Global	Africa	North America	South America	Spatiotemporal Resolution	Year of Fires	Reference
Equation (1)	3099–4159	1712–2654	164–405	145–181	month, 0.5°	2000	*Jain et al.* [2006]
Equation (1)	2797–3814	1824–2705	61–64	176–188	month, 1 km	2000	*Ito and Penner* [2004]
Equation (1)	2730–4056	NA[b]	NA	NA	month, 0.5°	2000	*Hoelzemann et al.* [2004]
Equation (1)	4539	2058	222	1407	month, 0.5°	2010	*van der Werf et al.* [2010]
Equation (2)	NA	855	NA	NA	day, 1°	2004	*Roberts et al.* [2009]
Equation (2)	NA	716	NA	NA	month, 0.5°	2001–2007	*Ellicott et al.* [2009]
Equation (2)	1326[c]	591	164	369	hour, pixel size	2010	This study

[a]Equation (1) represents the model based on burned area and biomass density (fuel loading) and equation (2) indicates the FRP method. The range of estimates in *Jain et al.* [2006] and *Ito and Penner* [2004] is the result of two different burned areas used.
[b]NA: Not available.
[c]No coverage for most regions in boreal Asia, the Middle East, and India.

et al., 2006; *Jain et al.*, 2006], which is much larger than some detailed field calculations [*Campbell et al.*, 2007; *Meigs et al.*, 2009]. It is likely that previous emission estimates commonly use combustion factor obtained from high-severity fires for all fire regimes, although low- and moderate-severity fires account for majority proportion in large wildfires [*Schwind*, 2008; *Miller et al.*, 2009; *Zhang et al.*, 2011].

[41] The FRP algorithm avoids the uncertainty in burned area, fuel loading, and combustion factor, but the results are influenced by FRP detection and biomass combustion rate (β). Although it is not easy to directly validate satellite FRP measurements, the FRP values detected from GOES Imager and Meteosat SEVERI have been shown to agree with MODIS FRP retrievals [*Roberts et al.*, 2005; *Xu et al.*, 2010]. However, at the regional scale SEVIRI typically underestimates FRP by up to 40% with respect to MODIS due primarily to its inability to confidently detect fire pixels with FRP $\leq$ 100 MW [*Roberts et al.*, 2005]. GOES FRP is undetected for many fire pixels having FRP < 30 MW and so GOES measurements could be on average 17% lower [*Xu et al.*, 2010].

[42] Moreover, the uncertainty of FRP in the GBBEP-Geo also comes from the satellite viewing angles. Fire characterization detections are based on the proportion of the pixel on fire. For pixels near the geostationary satellite limb, a larger fire area is necessary to create the same fire proportion as a pixel near the subsatellite point. As viewing angle increases, pixel size increases and the probability of detecting smaller and less intense fires decreases [*Giglio et al.*, 1999; *Freeborn et al.*, 2011]. As a result, the minimum detectable FRP increases toward the large viewing angles. Similar to MODIS FRE [*Freeborn et al.*, 2011], the viewing angle effect of geostationary satellites results in the underestimates of actual fire FRE. This effect is under investigation and will be included in the next version of GBBEP-Geo product.

[43] Although our simulated diurnal FRP values for a fire pixel are expected to compensate for fire detections without FRP calculations and some undetected fires, some uncertainties also exist. The shape of FRP diurnal pattern for individual fires varies slightly with different regions. Currently the climatological FRP shape generated using GOES fire detections in North America is applied to globe. After comparing the climatological pattern in North America with that in Africa during 2009 and 2010, we found the shape variation could cause an uncertainty of about 7%.

[44] The biomass combustion rate in FRE also causes certain uncertainty although it is shown not to vary with fuel types. Field controlled experiments (29 samples) demonstrate that the FRE combustion factor is 0.368 ± 0.015 kg/MJ regardless the land ecosystem types [*Wooster et al.*, 2005]. However, laboratory-controlled experiments in a combustion chamber demonstrate that the rate of dry fuels combusted per FRP unit ranges from 0.24 to 0.78 kg/MJ with an overall regression rate of 0.453 ± 0.068 kg/MJ [*Freeborn et al.*, 2008]. In GBBEP-Geo, we adopt the coefficient of 0.368 kg/MJ, which is 23% lower than the 0.453 kg/MJ.

[45] The above biomass combustion rate in FRE from laboratory-controlled experiments differs greatly from that obtained from other sources. In the GFASv0, the combustion rate is 1.37 kg/MJ that was obtained following a comparison of global MODIS FRE to emissions in GFED2 inventory [*Kaiser et al.*, 2009]. The aerosol optical thickness (AOT) simulated from FRE-based emissions (GFASv1.0) is lower than MODIS AOT by a factor of 3.4 [*Kaiser et al.*, 2012]. Similarly, the AOT simulated using MODIS FRE-derived fire emissions is less than MODIS AOT with factors of 1.8 in savannah and grasslands, 2.5 in tropical forest and 4.5 in extratropical forest [*Colarco et al.*, 2011]. This large discrepancy between bottom-up and top-down AOT estimates is unclear, which is likely caused by various factors that include the rapid changes of smoke particles with age [*Reid et al.*, 1998], the uncertainty in climate and atmospheric transport models, and underestimate of the biomass combustion factor and FRE.

[46] Moreover, the combustion rate in FRE is considerably large when comparing MODIS FRE with MODIS smoke AOT. The comparison indicates a FRE-based emission factor for total particulate mass (PM) is 0.02–0.06 kg/MJ for boreal regions, 0.04–0.08 kg/MJ for both tropical forests and savanna regions, and 0.08–0.1 kg/MJ for Western Russian regions [*Ichoku and Kaufman*, 2005]. If the rate of total PM emissions is converted to burned DM using PM2.5 emission factors in GFED3.1 [*van der Werf et al.*, 2010] and the ratio between total PM and PM2.5 [*Sofiev et al.*, 2009], the biomass combustion rate in FRE roughly ranges from 2 to 12 kg/MJ. However, these coefficients may be overestimated by about 50% [*Ichoku and Kaufman*, 2005]. Similarly, the emission coefficient for total PM in Europe is 0.035 kg/MJ for forest, 0.018 kg/MJ for grassland and agriculture, and 0.026 kg/MJ for mixed vegetation [*Sofiev et al.*, 2009]. These values are roughly associated to a biomass combustion rate of 1.6–2.2 kg/MJ. These results

indicate that the rate of biomass combustion in FRE from statistical comparisons between various data sets is much larger than that from laboratory-controlled experiments. We believe that the factor of converting FRE to biomass burning emissions needs further investigation.

[47] Emission factor is another source of the uncertainty in the estimates of biomass burning emissions. In regional and global scales, emission factors are highly aggregated to a few ecosystem types. Consequently, the values vary with the field measurements available and the ecosystem types classified [*Akagi et al.*, 2011; *van der Werf et al.*, 2010; *Wiedinmyer et al.*, 2006, 2011]. The uncertainty among these studies is consistent with that from field measurements for many important species, which is about 20–30% [*Andreae and Merlet*, 2001]. However, the emission factors of PM2.5 are about four times larger in various studies [e.g., *van der Werf et al.*, 2010; *Wiedinmyer et al.*, 2011] than those conducted by *Urbanski et al.* [2011]. Our GBBEP-Geo algorithm currently uses the factors from the literature [*Wiedinmyer et al.*, 2006], which is intended to updated using newly available data [*Akagi et al.*, 2011; *Wiedinmyer et al.*, 2011].

[48] Finally, the GBBEP-Geo does not produce biomass burning emissions from fires that occur in most regions of the Middle East, India and boreal Asia because of the lack of coverage from current geostationary satellites. For this region, boreal Asia is one of the most important fire regimes [*Soja et al.*, 2004], which releases 6.4% of global wildfire emissions [*van der Werf et al.*, 2010]. To overcome this limitation for investigating global biomass burning emissions, INSAT-3D, a geostationary satellite developed by the Indian Space Research Organization and expected to be launched in 2011, is expected to fill the gap.

5. Conclusions

[49] Fire radiative power estimated from multiple geostationary satellites provides an indispensable tool to calculate global biomass burning emissions in near real time on an hourly time scale. This product will significantly contribute to air quality and weather forecasting. The estimate of biomass burning emissions from FRP avoids using the complex parameters of fuel loading and burned area. Thus, it is a robust approach for the global estimates of biomass burning emissions. High frequent fire observations from geostationary satellites allow us to reconstruct the diurnal pattern in FRP for individual fire pixels. This increases the number of observations that otherwise would not be reported due to cloud/smoke cover.

[50] Note that high uncertainty exists in global biomass emissions and accurate validation is currently not possible because of the lack of reliable in situ measurement. Intercomposition among different products reveals that the FRP-based GBBEP-Geo estimates are generally smaller than previous global calculations from burned area and fuel loading with a factor of 2–3. However, GBBEP-Geo is comparable with emission estimates from GOES-based burned area and MODIS-based fuel loadings in the United States, from MODIS-based FRP, and from SEVERI-based FRP in Africa. Thus, it is evident that GBBEP-Geo produces reliable estimates of biomass burning emissions from wildfires. Finally, it should be noted that GBBEP-Geo currently provides limited coverage in high latitudes and no coverage in most regions across India and parts of boreal Asia.

[51] **Acknowledgments.** The authors thank Arlindo da Silva in NASA for providing QFED v1 data, Manajit Sengupta and Renate Brummer for fire proxy data, Gilberto Vicente for internal reviews, and four anonymous reviewers for constructive comments. The views, opinions, and findings contained in these works are those of the author(s) and should not be interpreted as an official NOAA or U.S. government position, policy, or decision.

References

Akagi, S. K., R. J. Yokelson, C. Wiedinmyer, M. J. Alvarado, J. S. Reid, T. Karl, J. D. Crounse, and P. O. Wennberg (2011), Emission factors for open and domestic biomass burning for use in atmospheric models, *Atmos. Chem. Phys.*, *11*, 4039–4072, doi:10.5194/acp-11-4039-2011.

Al-Saadi, J., et al. (2008), Intercomparison of near-real-time biomass burning emissions estimates constrained by satellite fire data, *J. Appl. Remote Sens.*, *2*, 021504, doi:10.1117/1.2948785.

Anderson, G. K., D. V. Sandberg, and R. A. Norheim (2004), Fire Emission Production Simulator (FEPS) user's guide, version 1.0, For. Serv., U.S. Dep. of Agric., Portland, Oreg. [Available at http://www.fs.fed.us/pnw/fera/publications/fulltext/FEPS_User_Guide.pdf.]

Andreae, M. O., and P. Merlet (2001), Emission of trace gases and aerosols from biomass burning, *Global Biogeochem. Cycles*, *15*(4), 955–966, doi:10.1029/2000GB001382.

Beck, J. A., and A. C. F. Trevitt (1989), Forecasting diurnal variations in meteorological parameters for predicting fire behaviour, *Can. J. For. Res.*, *19*, 791–797, doi:10.1139/x89-120.

Beck, J. A., M. E. Alexander, S. D. Harvey, and A. K. Beaver (2001), Forecasting diurnal variation in fire intensity for use in wildland fire management applications, paper presented at Fourth Symposium on Fire and Forest Meteorology, Am. Meteorol. Soc., Reno, Nev., 13–15 Nov.

Boschetti, L., H. D. Eva, P. A. Brivio, and J. M. Grégoire (2004), Lessons to be learned from the comparison of three satellite-derived biomass burning products, *Geophys. Res. Lett.*, *31*, L21501, doi:10.1029/2004GL021229.

Brown, J. F., T. R. Loveland, D. O. Ohlen, and Z. Zhu (1999), The global land-cover characteristics data-base: The users' perspective, *J. Am. Soc. Photogramm. Remote Sens.*, *65*(9), 1069–1074.

Campbell, J., D. Donato, D. Azuma, and B. Law (2007), Pyrogenic carbon emission from a large wildfire in Oregon, United States, *J. Geophys. Res.*, *112*, G04014, doi:10.1029/2007JG000451.

Chin, M., T. Diehl, P. Ginoux, and W. Malm (2007), Intercontinental transport of pollution and dust aerosols: Implications for regional air quality, *Atmos. Chem. Phys.*, *7*, 5501–5517, doi:10.5194/acp-7-5501-2007.

Cochrane, M. A. (2003), Fire science for rainforests, *Nature*, *421*, 913–919, doi:10.1038/nature01437.

Colarco, P., et al. (2011), The NASA GEOS-5 aerosol forecasting system, paper presented at the MACC Conference on Monitoring and Forecasting Atmospheric Composition, Eur. Cent. for Medium Range Weather Forecasts, Utrecht, Netherlands, 23–27 May.

Conard, S. G., A. I. Sukhinin, B. J. Stocks, D. R. Cahoon, E. P. Davidenko, and G. A. Ivanova (2002), Determining effects of area burned and fire severity on carbon cycling and emissions in Siberia, *Clim. Change*, *55*, 197–211.

Ellicott, E., E. Vermote, L. Giglio, and G. Roberts (2009), Estimating biomass consumed from fire using MODIS FRE, *Geophys. Res. Lett.*, *36*, L13401, doi:10.1029/2009GL038581.

Freeborn, P. H., M. J. Wooster, W. M. Hao, C. A. Ryan, B. L. Nordgren, S. P. Baker, and C. Ichoku (2008), Relationships between energy release, fuel mass loss, and trace gas and aerosol emissions during laboratory biomass fires, *J. Geophys. Res.*, *113*, D01301, doi:10.1029/2007JD008679.

Freeborn, P. H., M. J. Wooster, and G. Roberts (2011), Addressing the spatiotemporal sampling design of MODIS to provide estimates of the fire radiative energy emitted from Africa, *Remote Sens. Environ.*, *115*, 475–489, doi:10.1016/j.rse.2010.09.017.

French, N. H. F., et al. (2011), Model comparisons for estimating carbon emissions from North American wildland fire, *J. Geophys. Res.*, *116*, G00K05, doi:10.1029/2010JG001469.

Galanter, M., H. Levy II, and G. R. Carmichael (2000), Impacts of biomass burning on tropospheric CO, NO_x, and O_3, *J. Geophys. Res.*, *105*, 6633–6653.

Giglio, L. (2007), Characterization of the tropical diurnal fire cycle using VIRS and MODIS observations, *Remote Sens. Environ.*, *108*, 407–421, doi:10.1016/j.rse.2006.11.018.

Giglio, L., J. D. Kendall, and C. O. Justice (1999), Evaluation of global fire detection algorithms using simulated AVHRR infrared data, *Int. J. Remote Sens.*, *20*, 1947–1985, doi:10.1080/014311699212290.

Giglio, L., J. D. Kendall, and R. Mack (2003), A multi-year active fire dataset for the tropics derived from the TRMM VIRS, *Int. J. Remote Sens.*, *24*, 4505–4525.

Giglio, L., T. Loboda, D. P. Roy, B. Quayle, and C. O. Justice (2009), An active-fire based burned area mapping algorithm for the MODIS sensor, *Remote Sens. Environ.*, *113*, 408–420, doi:10.1016/j.rse.2008.10.006.

Giglio, L., J. T. Randerson, G. R. van der Werf, P. S. Kasibhatla, G. J. Collatz, D. C. Morton, and R. S. DeFries (2010), Assessing variability and long-term trends in burned area by merging multiple satellite fire products, *Biogeosciences*, *7*, 1171–1186, doi:10.5194/bg-7-1171-2010.

Grasso, L., M. Sengupta, and D. T. Lindsey (2008), Synthetic GOES-R imagery development and uses, paper presented at Fifth GOES Users' Conference, NOAA, New Orleans, La., 23–24 Jan.

Hao, W. M., and M.-H. Liu (1994), Spatial and temporal distribution of tropical biomass burning, *Global Biogeochem. Cycles*, *8*, 495–503.

Hao, W. M., M.-H. Liu, and P. J. Crutzen (1990), Estimates of annual and regional releases of CO_2 and other trace gases to the atmosphere from fires in the tropics, based on the FAO statistics for the period 1975–80, in *Fire in the Tropical Biota: Ecosystem Processes and Global Challenges*, *Ecol. Stud.*, vol. 84, edited by J. G. Goldammer, pp. 440–462, Springer, New York.

Hillger, D., M. DeMaria, R. Brummer, L. Grasso, M. Sengupta, and R. DeMaria (2009), Production of proxy datasets in support of GOES-R algorithm development, *Proc. SPIE Int. Soc. Opt. Eng.*, *7458*, 74580C, doi:10.1117/12.828489.

Hoelzemann, J. J., M. G. Schultz, G. P. Brasseur, C. Granier, and M. Simon (2004), Global Wildland Fire Emission Model (GWEM): Evaluating the use of global area burnt satellite data, *J. Geophys. Res.*, *109*, D14S04, doi:10.1029/2003JD003666.

Ichoku, C., and Y. J. Kaufman (2005), A method to derive smoke emission rates from MODIS fire radiative energy measurements, *IEEE Trans. Geosci. Remote Sens.*, *43*(11), 2636–2649, doi:10.1109/TGRS.2005.857328.

Ichoku, C., L. Giglio, M. J. Wooster, and L. A. Remer (2008), Global characterization of biomass-burning patterns using satellite measurements of fire radiative energy, *Remote Sens. Environ.*, *112*, 2950–2962, doi:10.1016/j.rse.2008.02.009.

Ito, A., and J. E. Penner (2004), Global estimates of biomass burning emissions based on satellite imagery for the year 2000, *J. Geophys. Res.*, *109*, D14S05, doi:10.1029/2003JD004423.

Jain, A. K., Z. Tao, X. Yang, and C. Gillespie (2006), Estimates of global biomass burning emissions for reactive greenhouse gases (CO, NMHCs, and NO_x) and CO_2, *J. Geophys. Res.*, *111*, D06304, doi:10.1029/2005JD006237.

Justice, C. O., J. R. G. Townshend, E. F. Vermote, E. Masuoka, R. E. Wolfe, N. Saleous, D. P. Roy, and J. T. Morisette (2002), An overview of MODIS land data processing and product status, *Remote Sens. Environ.*, *83*, 3–15.

Kaiser, J. W., J. Flemming, M. G. Schultz, M. Suttie, and M. J. Wooster (2009), The MACC global fire assimilation system: First emission products (GFASv0), *ECMWF Tech. Memo. 596*, 18 pp., Eur. Cent. for Medium Range Weather Forecasts, Reading, U. K.

Kaiser, J. W., et al. (2012), Biomass burning emissions estimated with a global fire assimilation system based on observed fire radiative power, *Biogeosciences*, *9*, 527–554, doi:10.5194/bg-9-527-2012.

Kaufman, Y. J., C. O. Justice, L. P. Flynn, J. D. Kendall, E. M. Prins, L. Giglio, D. E. Ward, W. P. Menzel, and A. W. Setzer (1998), Potential global fire monitoring from EOS-MODIS, *J. Geophys. Res.*, *103*(D24), 32,215–32,238, doi:10.1029/98JD01644.

Langenfelds, R. L., R. J. Francey, B. C. Pak, L. P. Steele, J. Lloyd, C. M. Trudinger, and C. E. Allison (2002), Interannual growth rate variations of atmospheric CO_2 and its $\delta^{13}C$, H_2, CH_4, and CO between 1992 and 1999 linked to biomass burning, *Global Biogeochem. Cycles*, *16*(3), 1048, doi:10.1029/2001GB001466.

Lobert, J., and J. Warnatz (1993), Emissions from the combustion process in vegetation, in *Fire in the Environment: The Ecological, Atmospheric, and Climatic Importance of Vegetation Fires*, *Environ. Sci. Res. Rep.*, vol. 13, edited by P. J. Crutzen and J. G. Goldammer, pp. 15–39, John Wiley, New York.

Lobert, J. M., W. C. Keene, J. A. Logan, and R. Yevich (1999), Global chlorine emissions from biomass burning: Reactive Chlorine Emissions Inventory, *J. Geophys. Res.*, *104*, 8373–8389.

Meigs, G. W., D. C. Donato, J. L. Campbell, J. G. Martin, and B. E. Law (2009), Forest fire impacts on carbon uptake, storage, and emission: The role of burn severity in the eastern Cascades, Oregon, *Ecosystems*, *12*(8), 1246–1267, doi:10.1007/s10021-009-9285-x.

Miller, J. D., H. D. Safford, M. Crimmins, and A. E. Thode (2009), Quantitative evidence for increasing forest fire severity in the Sierra Nevada and southern Cascade Mountains, California and Nevada, USA, *Ecosystems*, *12*, 16–32, doi:10.1007/s10021-008-9201-9.

Mu, M., et al. (2011), Daily and 3-hourly variability in global fire emissions and consequences for atmospheric model predictions of carbon monoxide, *J. Geophys. Res.*, *116*, D24303, doi:10.1029/2011JD016245.

Piccolini, I., and O. Arino (2000), Towards a global burned surface world atlas, *Earth Obs. Q.*, *65*, 14–18.

Plummer, S., O. Arino, M. Simon, and W. Steffen (2006), Establishing a Earth observation product service for the terrestrial carbon community: The Globcarbon Initiative, *Mitigation Adaptation Strategies Global Change*, *11*, 97–111.

Prins, E. M., and W. P. Menzel (1992), Geostationary satellite detection of biomass burning in South America, *Int. J. Remote Sens.*, *13*, 2783–2799.

Prins, E. M., J. M. Feltz, W. P. Menzel, and D. E. Ward (1998), An overview of GOES-8 diurnal fire and smoke results for SCAR-B and 1995 fire season in South America, *J. Geophys. Res.*, *103*(D24), 31,821–31,835, doi:10.1029/98JD01720.

Reid, J. S., P. V. Hobbs, R. J. Ferek, D. R. Blake, J. V. Martins, M. R. Dunlap, and C. Liousse (1998), Physical, chemical, and optical properties of regional hazes dominated by smoke in Brazil, *J. Geophys. Res.*, *103*, 32,059–32,080, doi:10.1029/98JD00458.

Reid, J. S., E. M. Prins, D. L. Westphal, C. C. Schmidt, K. A. Richardson, S. A. Christopher, T. F. Eck, E. A. Reid, C. A. Curtis, and J. P. Hoffman (2004), Real-time monitoring of South American smoke particle emissions and transport using a coupled remote sensing/box-model approach, *Geophys. Res. Lett.*, *31*, L06107, doi:10.1029/2003GL018845.

Roberts, G., M. J. Wooster, G. L. W. Perry, N. Drake, L.-M. Rebelo, and F. Dipotso (2005), Retrieval of biomass combustion rates and totals from fire radiative power observations: Application to southern Africa using geostationary SEVIRI imagery, *J. Geophys. Res.*, *110*, D21111, doi:10.1029/2005JD006018.

Roberts, G., M. J. Wooster, and E. Lagoudakis (2009), Annual and diurnal African biomass burning temporal dynamics, *Biogeosciences*, *6*, 849–866, doi:10.5194/bg-6-849-2009.

Rothermel, R. C., and R. W. Mutch (1986), Behavior of the life-threatening Butte fire: August 27–29, 1985, *Fire Manage. Notes*, *47*(2), 14–24.

Roy, D. P., and L. Boschetti (2009), Southern Africa validation of the MODIS, L3JRC, and GlobCarbon burned-area products, *IEEE Trans. Geosci. Remote Sens.*, *47*, 1032–1044, doi:10.1109/TGRS.2008.2009000.

Roy, D. P., P. E. Lewis, and C. O. Justice (2002), Burned area mapping using multi-temporal moderate spatial resolution data—A bi-directional reflectance model-based expectation approach, *Remote Sens. Environ.*, *83*(1–2), 263–286.

Roy, D. P., L. Boschetti, C. O. Justice, and J. Ju (2008), The collection 5 MODIS burned area product—Global evaluation by comparison with the MODIS active fire product, *Remote Sens. Environ.*, *112*(9), 3690–3707.

Schmidt, C. C., and E. M. Prins (2003), GOES wildfire ABBA applications in the Western Hemisphere, paper presented at the Second International Wildland Fire Ecology and Fire Management Congress, Am. Meteorol. Soc., Orlando, Fla., 16–20 Nov.

Schmidt, C. C., J. Hoffman, E. Prins, and S. Lindstrom (2010), GOES-R advanced baseline imager (ABI) algorithm theoretical basis document for fire/hot spot characterization, version 2.0, NOAA, Silver Spring, Md. [Available at http://www.goes-r.gov/products/ATBDs/baseline/baseline-fire-hot-spot-v2.0.pdf.]

Schroeder, M. J., and C. C. Buck (1970), Fire weather—A guide for application of meteorological information to forest fire control operations, *Agric. Handb. 360*, 229 pp., For. Serv., U.S. Dep. of Agric., Washington, D. C.

Schwind, B. (Comp.) (2008), Monitoring trends in burn severity: Report on the Pacific Northwest and Pacific Southwest fires (1984 to 2005), U.S. Geol. Surv., Reston, Va. [Available at http://mtbs.gov.]

Seiler, W., and P. J. Crutzen (1980), Estimates of gross and net fluxes of carbon between the biosphere and the atmosphere from biomass burning, *Clim. Change*, *2*, 207–247, doi:10.1007/BF00137988.

Simon, M., S. Plummer, F. Fierens, J. J. Hoelzemann, and O. Arino (2004), Burnt area detection at global scale using ATSR-2: The GLOBSCAR products and their qualification, *J. Geophys. Res.*, *109*, D14S02, doi:10.1029/2003JD003622.

Sofiev, M., R. Vankevich, M. Lotjonen, M. Prank, V. Petukhov, T. Ermakova, J. Koskinen, and J. Kukkonen (2009), An operational system for the assimilation of the satellite information on wild-land fires for the needs of air quality modelling and forecasting, *Atmos. Chem. Phys.*, *9*, 6833–6847, doi:10.5194/acp-9-6833-2009.

Soja, A. J., W. R. Cofer, H. H. Shugart, A. I. Sukhinin, P. W. Stackhouse Jr., D. J. McRae, and S. G. Conard (2004), Estimating fire emissions

and disparities in boreal Siberia (1998–2002), *J. Geophys. Res.*, *109*, D14S06, doi:10.1029/2004JD004570.

Tansey, K., J.-M. Grégoire, P. Defourny, R. Leigh, J.-F. Pekel, E. van Bogaert, and E. Bartholomé (2008), A new, global, multi-annual (2000–2007) burnt area product at 1 km resolution, *Geophys. Res. Lett.*, *35*, L01401, doi:10.1029/2007GL031567.

Trollope, W. S. W., L. A. Trollope, A. L. F. Potgieter, and N. Zambatis (1996), SAFARI-92 characterization of biomass and fire behavior in the small experimental burns in Kruger National Park, *J. Geophys. Res.*, *101*, 23,531–23,539, doi:10.1029/96JD00691.

Urbanski, S. P., W. M. Hao, and B. Nordgren (2011), The wildland fire emission inventory: Western United States emission estimates and an evaluation of uncertainty, *Atmos. Chem. Phys.*, *11*, 12,973–13,000, doi:10.5194/acp-11-12973-2011.

van der Werf, G. R., J. T. Randerson, L. Giglio, G. J. Collatz, P. S. Kasibhatla, and A. F. Arellano Jr. (2006), Interannual variability in global biomass burning emissions from 1997 to 2004, *Atmos. Chem. Phys.*, *6*(11), 3423–3441.

van der Werf, G. R., J. T. Randerson, L. Giglio, G. J. Collatz, M. Mu, P. S. Kasibhatla, D. C. Morton, R. S. DeFries, Y. Jin, and T. T. van Leeuwen (2010), Global fire emissions and the contribution of deforestation, savanna, forest, agricultural, and peat fires (1997–2009), *Atmos. Chem. Phys. Discuss.*, *10*, 16,153–16,230, doi:10.5194/acpd-10-16153-2010.

Weaver, J. F., D. Lindsey, D. Bikos, C. C. Schmidt, and E. Prins (2004), Fire detection using GOES rapid scan imagery, *Weather Forecasting*, *19*, 496–510, doi:10.1175/1520-0434(2004)019<0496:FDUGRS>2.0.CO;2.

Whelan, R. J. (1995), *The Ecology of Fire*, Cambridge Univ. Press, New York.

Wiedinmyer, C., B. Quayle, C. Geron, A. Belote, D. McKenzie, X. Zhang, S. O'Neill, and K. K. Wynne (2006), Estimating emissions from fires in North America for air quality modeling, *Atmos. Environ.*, *40*, 3419–3432, doi:10.1016/j.atmosenv.2006.02.010.

Wiedinmyer, C., S. K. Akagi, R. J. Yokelson, L. K. Emmons, J. A. Al-Saadi, J. J. Orlando, and A. J. Soja (2011), The Fire INventory from NCAR (FINN): A high resolution global model to estimate the emissions from open burning, *Geosci. Model Dev.*, *4*, 625–641, doi:10.5194/gmd-4-625-2011.

Wooster, M. J. (2002), Small-scale experimental testing of fire radiative energy for quantifying mass combusted in natural vegetation fires, *Geophys. Res. Lett.*, *29*(21), 2027, doi:10.1029/2002GL015487.

Wooster, M. J., B. Zhukov, and D. Oertel (2003), Fire radiative energy for quantitative study of biomass burning: Derivation from the BIRD experimental satellite and comparison to MODIS fire products, *Remote Sens. Environ.*, *86*, 83–107, doi:10.1016/S0034-4257(03)00070-1.

Wooster, M. J., G. Roberts, G. L. W. Perry, and Y. J. Kaufman (2005), Retrieval of biomass combustion rates and totals from fire radiative power observations: FRP derivation and calibration relationships between biomass consumption and fire radiative energy release, *J. Geophys. Res.*, *110*, D24311, doi:10.1029/2005JD006318.

Xu, W., M. J. Wooster, G. Roberts, and P. Freeborn (2010), New GOES imager algorithms for cloud and active fire detection and fire radiative power assessment across North, South and Central America, *Remote Sens. Environ.*, *114*, 1876–1895, doi:10.1016/j.rse.2010.03.012.

Yang, E.-S., S. A. Christopher, S. Kondragunta, and X. Zhang (2011), Use of hourly Geostationary Operational Environmental Satellite (GOES) fire emissions in a Community Multiscale Air Quality (CMAQ) model for improving surface particulate matter predictions, *J. Geophys. Res.*, *116*, D04303, doi:10.1029/2010JD014482.

Zhang, X., and S. Kondragunta (2006), Estimating forest biomass in the USA using generalized allometric models and MODIS land products, *Geophys. Res. Lett.*, *33*, L09402, doi:10.1029/2006GL025879.

Zhang, X., and S. Kondragunta (2008), Temporal and spatial variability in biomass burned areas across the USA derived from the GOES fire product, *Remote Sens. Environ.*, *112*, 2886–2897, doi:10.1016/j.rse.2008.02.006.

Zhang, X., M. A. Friedl, C. B. Schaaf, A. H. Strahler, and Z. Liu (2005), Monitoring the response of vegetation phenology to precipitation in Africa by coupling MODIS and TRMM instruments, *J. Geophys. Res.*, *110*, D12103, doi:10.1029/2004JD005263.

Zhang, X., S. Kondragunta, C. Schmidt, and F. Kogan (2008), Near real time monitoring of biomass burning particulate emissions (PM2.5) across contiguous United States using multiple satellite instruments, *Atmos. Environ.*, *42*, 6959–6972, doi:10.1016/j.atmosenv.2008.04.060.

Zhang, X., S. Kondragunta, and B. Quayle (2011), Estimation of biomass burned areas using multiple-satellite-observed active fires, *IEEE Trans. Geosci. Remote Sens.*, *49*, 4469–4482, doi:10.1109/TGRS.2011.2149535.